QUANTIFYING LAND SUBSIDENCE RATES IN THE COASTAL BEND OF TEXAS USING TEMPORAL GRAVIMETRY, CAMPAIGN AND PERMANENT GNSS, AND INTERFEROMETRIC RADAR TECHNIQUES

A Thesis

by

AMANDA BEATTIE

BS, Texas A&M University - Corpus Christi, 2020

Submitted in Partial Fulfillment of the Requirements for the Degree of

MASTER OF SCIENCE

in

ENVIRONMENTAL SCIENCE

Texas A&M University-Corpus Christi
Corpus Christi, Texas

December 2022

December 2022

QUANTIFYING LAND SUBSIDENCE RATES IN THE COASTAL BEND OF TEXAS USING TEMPORAL GRAVIMETRY, CAMPAIGN AND PERMANENT GNSS, AND INTERFEROMETRIC RADAR TECHNIQUES

A Thesis

by

AMANDA BEATTIE

This thesis meets the standards for scope and quality of
Texas A&M University-Corpus Christi and is hereby approved.

Mohamed Ahmed, PhD
Chair

Tianxing Chu, PhD
Committee Member

Esayas Gebremichael, PhD
Committee Member

December 2022

ABSTRACT

Land subsidence and local sea level rise are well-known, ongoing problems that are negatively impacting the Coastal Bend of Texas. Land subsidence in this area increases the vulnerability of coastal communities to effects of flood and hurricane events. In this study, four different approaches were used for quantifying land subsidence rates over the Coastal Bend of Texas on both local and regional scales. The first approach was a gravity survey, which employed a relative gravimeter to measure temporal gravity changes every two weeks for a period of two years (Oct. 2020 – Sept. 2022) on a local scale over six different areas around Corpus Christi, North Padre Island, Mustang Island, and Rockport. The second approach was to utilize campaign Global Navigation Satellite System (GNSS) elevation measurements, which were collected in a campaign congruent with the gravity survey. The third approach used the Interferometric Synthetic Aperture Radar (InSAR) to generate land deformation rates over the central Coastal Bend region on a reginal scale during from January 2017 to November 2021. The fourth approach used fifteen permanent GNSS stations to quantify land subsidence rates on a regional scale over a time period similar to that of the InSAR. The gravity- and campaign GNSS-derived deformation rates were compared with each other, while the InSAR and permanent GNSS rates were compared. Factors driving InSAR-derived subsidence rates were also investigated.

While both local and regional integrations showed significant correlation, land subsidence results from the gravity and campaign GNSS surveys could be enhanced with an extended campaign period and more frequent data acquisition. Additionally, the gravity-derived land subsidence rates could be improved by selecting a more stable base station location, utilizing high-precision relative gravimeter and/or an absolute gravimeter, and target a noise-free acquisition days and times. The InSAR-derived rates were consistent with the permanent GNSS-derived rates (R: 0.7). Results of this study showed that land subsidence rates exhibited spatial and temporal variations across the Coastal Bend of Texas. Four regions were identified to experience significant InSAR-derived land subsidence rates: inland towns (total: 17); coastal towns (total: 6); cities (total: 6); industrial plants (total: 8). Four coastal towns subsided at an average rate of -2 ± 3 mm/yr (range: -4 ± 4 to -0.4 ± 3 mm/yr), likely driven by sediment compaction and growth faulting. Three regions classified as city around the Corpus Christi urban area experienced an average subsidence rate of -2 ± 3 mm/yr (range: -4 ± 3 to -0.2 ± 3 mm/yr), with subsidence being attributed to increased groundwater extraction rates, sediment compaction, and growth faulting. Three inland towns experienced average subsidence rates of -4 ± 4 mm/yr (range: -8 ± 8 to -0.7 ± 3 mm/yr); two inland towns close in proximity to the coastline experienced subsidence that is likely attributed to a high density of growth faults, while the town located further inland could have experienced subsidence due to enhanced groundwater extraction activities. Seven industrial plants experienced subsidence at an average rate of -4 ± 6 mm/yr (range: -8 ± 6 mm/yr to -0.2 ± 5 mm/yr). The localized subsidence observed within these areas is thought to be driven by sediment compaction by overburden from storage tanks. Quantifying land subsidence is important in estimating local sea-level rise, determining the local geoid, and improving understanding of their controlling factors. Land subsidence rates, generated from this study, could be useful for supporting coastal communities in mitigating the effects of natural forces and improving their resilience against them.

DEDICATION

To my mom, who always cheered for me, cried with me, and fought for me. To my brother, whose quiet and steadfast support means more than he could ever know. To my sister, my soulmate, who was at my side every single moment of the way. To my compassionate best friend, who took care of me when I was at my lowest. To my devoted fiancé, my pillar, whose love and sacrifice made it possible to carry this through to the end.

And to my dad, who has endlessly loved me, encouraged me, and supported me in every possible way. I have only come this far because of you.

ACKNOWLEDGEMENTS

First, I would like to thank my advisor and mentor Dr. Mohamed Ahmed for his patience, guidance, encouragement, and support. He challenged me to push myself and test the full scope of my ability. Because of him, I am a better scientist and a better person. Second, thanks to my committee members Dr. Tianxing Chu and Dr. Esayas Gebremichael for their expertise and support. They helped me cultivate my work into something I can be proud of. My committee made this study possible, and their guidance and encouragement helped me go above and beyond in seeing this project through to the end. Third, I would like to thank the NGS Program and CBI for logistics and continuous support over the past two years. And lastly, a special thanks to Michael Haley, Michael Kleine, and Muhamed Elshalkany for continuously helping me with field measurements.

This study was prepared by Texas A&M University-Corpus Christi using Federal funds under award NA18NOS4000198 from the National Oceanic and Atmospheric Administration, U.S. Department of Commerce. The statements, findings, conclusions, and recommendations are those of the author(s) and do not necessarily reflect the views of the National Oceanic and Atmospheric Administration or the U.S. Department of Commerce.

TABLE OF CONTENTS

LIST OF FIGURES

LIST OF TABLES

CHAPTER I

INTRODUCTION, OBJECTIVES AND SIGNIFICANCE

1.1 Introduction

Approximately 25% of the continental U.S. is classified as coastal area, and these areas are twice as developed as interior areas of the country, which accounts for 40% of the nation's population. Since 1970, the coastal shoreline counties have seen a 39% population increase (NOAA, 2013). A 3% of these coastal counties can be classified in the low elevation coastal zone, which is defined as the contiguous area along the coast that is less than ten meters above sea level (Mcgranahan et al. 2007). Low lying coastal areas face heightened vulnerability due to coastal flooding caused by extreme astronomical tides, tsunamis, storm surge, and consistently rising sea level (Wu et al. 2002). In addition to vulnerability to the effects of coastal flooding, these low lying areas are susceptible to the hazard of land subsidence, commonly defined as the gentle settling or sudden sinking of the Earth's surface due to removal or displacement of subsurface materials (Galloway & Burbey, 2011). Though common across many different regions around the globe, subsidence poses a serious threat to coastal communities as it increases their already heightened vulnerability to flooding events resulting from cyclones, tidal events, tsunamis, and sea-level rise (Dolan and Walker 2006; Felsenstein and Lichter 2014).

Sea level variations can result from both eustatic changes in the ocean level or vertical land movements (Warrick and Oerlemans 1990). Relative sea level rise (RSLR) increases the severity of flooding, and it is associated with coastal erosion, loss of wetland habitat, permanent inundation of deltas and emergent land, the inland migration of barrier islands, and saltwater intrusion in both surface water and coastal aquifers (Don et al. 2006; Fitzgerald et al. 2008). Coastal land, specifically barrier islands and wetlands, play a large role in protecting urban areas from damaging effects of large storms. Land loss leaves these urban areas more vulnerable to extreme weather events. Hurricanes (specifically the associated storm surge hazard to low-lying land) results in damage to infrastructure, loss of life and agricultural product, and contamination of fresh water resources (Emanuel 2005; Venkataramanan et al. 2019; Haley et al. 2022). As such, land subsidence is a major factor controlling the response of coastal communities to these climate related hazards.

From an infrastructure/urban development perspective, subsidence also poses several problems. Subsidence can cause surface faults and slope failure, which can be damaging to vital urban framework like housing, railways, bridges, and other infrastructure. Damage to utility and infrastructure results in communities spending funds and time repaving roads, correcting foundational issues, replacing damaged utilities, and implementing mitigation measures to combat hazard areas. Additionally, it is difficult to incorporate the effects of subsidence into policy and engineering plans, a problem which likely stems from the complexity of the factors that drive subsidence as well as the wide range and gradient of subsidence rates (Yuill et al. 2009; Pacheco-Martínez et al. 2015). As subsidence poses problems to all coastal communities, it is important to determine the rates, locations, and factors controlling this phenomenon.

Land subsidence occurs through a variety of both natural and anthropogenic drivers (Figure 1). The six primary categories of subsidence processes include fluid withdrawal, tectonics (growth faulting and salt movement), sediment compaction, sediment loading, surface water drainage and management, and glacial isostatic adjustment (Yuill et al. 2009).

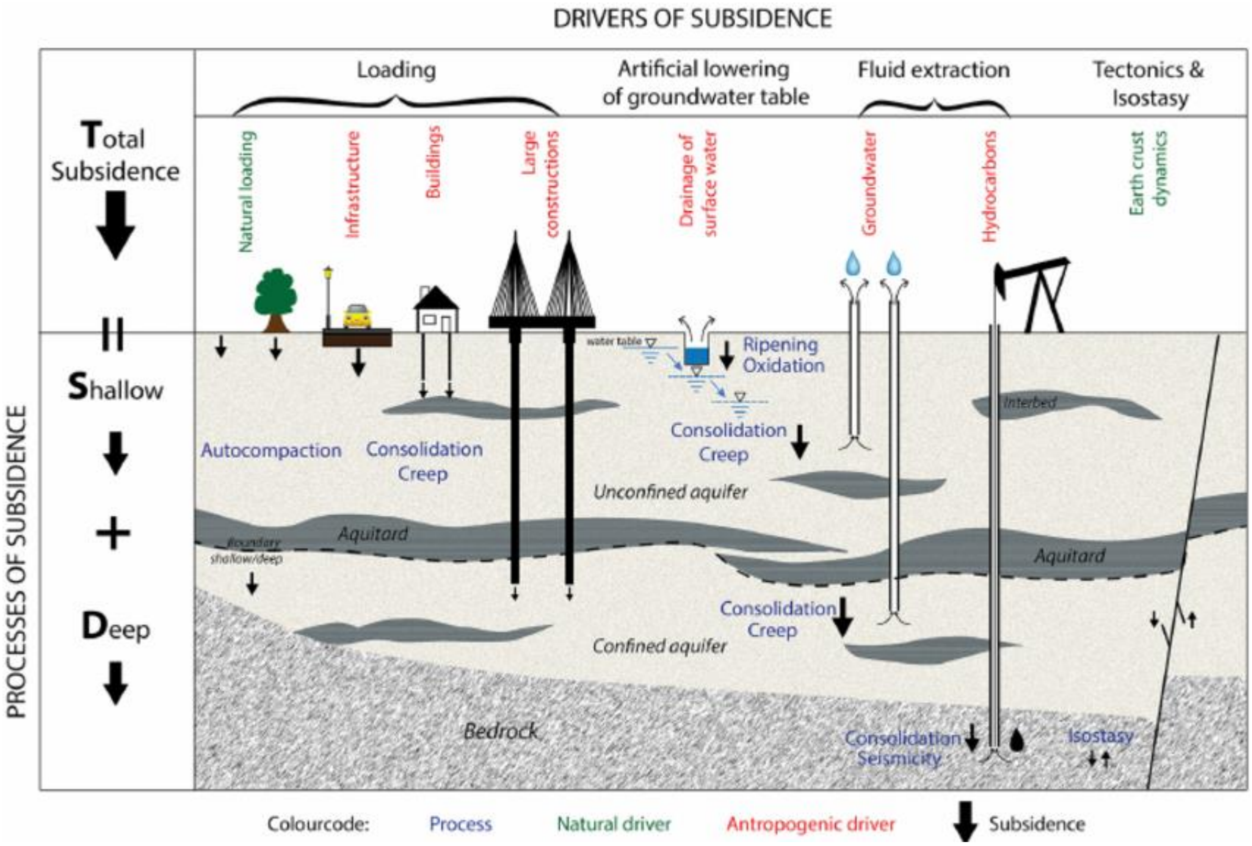

Figure 1:Conceptual model of the processes of subsidence, as well as the factors that drive it (Minderhoud et al., 2015).

1.2 Factors Controlling Land Subsidence

Fluid Withdrawal- Fluid withdrawal is one of the most common driving factors of subsidence. In this anthropogenic process, subsidence is caused by reservoir compaction as fluid withdrawal reduces subsurface pore pressure (Donaldson et al. 1995). This can be due to groundwater or hydrocarbon extraction.

Tectonics- Growth faulting and salt movement (halokinesis) can drive subsidence. Growth faulting can be due to deltaic construction or extension over the continental shelf edge. As the sediments spread over inclined layers, growth faults form as zones slip over time due to gravitational slumping (Galloway, 1986; Yuill et al., 2009). The phenomenon of salt movement occurs when sediments overlay salt deposits, and then salt diapirs rise due to their relatively low density compared to the density of surrounding sediments (Jackson 1995). This movement creates fault slips.

Sediment Compaction- Sediment compaction is influenced by sediment type, porosity, grain size, and water content. As grains settle, sediment volume is reduced and sediment density increases. Sediment compaction can occur naturally through mechanical processes such as overburden loading and glacial isostatic adjustment, or anthropogenically through fluid withdrawal (van Asselen et al. 2009; Haley et al. 2022).

1.3 Investigating Land Subsidence

Quantifying land subsidence is important in estimating local sea-level rise, determining the local geoid, and supporting coastal communities in mitigating the effects of natural interventions and improving the resilience against these forces. Land subsidence can be observed and measured in a variety of ways. Continuously operating global navigation satellite systems (GNSS) provide accurate (though spatially limited) rates of subsidence (Yu and Wang 2016). Satellite altimetry and remote sensing with interferometric synthetic aperture radar (InSAR) can provide rates of crustal displacement over a widespread area (Moreira et al. 2013). A gravity survey can also be useful in determining land surface deformation in detail around focused areas (Torge 1986).

1.3.1 Remote Sensing for Investigating Subsidence

Over the past 30 years, the use of satellite Synthetic Aperture Radar (SAR) imagery and techniques for monitoring surface deformation has become widespread. SAR methods include differential Interferometric Synthetic Aperture Radar and multi-temporal InSAR (Cigna and Tapete 2021). This remote sensing technique uses multi-temporal radar image pairs to generate interference patterns when differing radar wave phases are detected over the same location. Between acquisitions, the satellite detects whether the target area moved toward or away from the satellite, implying either uplift or subsidence respectively, and the resulting distance changes can be used to generate surface deformation maps (Lu et al., 2007.).

1.3.2 Geophysical Techniques for Investigating Subsidence

While InSAR is able to provide widespread spatial coverage as well as a comprehensive view of land surface deformation rates on a larger scale, a gravity survey is useful in determining land surface deformation in focused local-scale areas. Gravimetry can be used to monitor vertical crustal movement due to density changes, elevation changes, or changes in mass distribution (Issawy et al. 2010). By creating a survey loop that begins and ends at a reference base station, relative gravity measurements can be obtained at different locations and used to measure the rates of deformation (Torge 1986).

1.3.4 Geomatic Techniques for Investigating Subsidence

Historically, land deformation has been monitored by leveling surveys at established benchmarks, from permanent Global Navigation Satellite System (GNSS) stations, and campaign GNSS surveys. For permanent GNSS stations, made available in the U.S. through Continuously Operating Reference Stations (CORS) network, there are over 1,000 located just within the Gulf Coastal Plain (Zhou et al. 2021), with some having an operational history dating to the early 2000's. These stations record measurements spanning from 5 minutes to 24 hours, and they provide vertical displacement time series as well as three dimensional coordinates. The generated data sets from these stations are available to the public through the National Geodetic Survey and University Navigation Satellite Timing & Ranging (NAVSTAR) Consortium (UNAVCO) (Zhou et al. 2021).

1.4 Objectives and Significance

The purpose of this study is to quantify the rate of land subsidence in the Coastal Bend of Texas using InSAR, gravimetry, and campaign and permanent GNSS data . By integrating the aforementioned methods, new datasets will be generated that can be used to examine the spatial and temporal variability of subsidence rates around the Coastal Bend of Texas. This will allow for the methods to be compared to determine the limitations and advantages of each technique. Additionally, this study can generate conceptual models that can work to explain and investigate the factors contributing to any observed subsidence rates and locations.

Land subsidence is a persisting phenomenon along the Texas coast that is detrimental to coastal communities by making them more vulnerable to climate related changes such as flooding from storm surges resulting from extreme weather events and gradual inundation from high sea-level rise rates. Determining the rates of land subsidence can help delineate areas are more prone to coastal hazards that are induced by subsidence. By determining the rates and locations of high variability of land subsidence, steps can be taken by the community to mitigate these hazards by reinforcing their infrastructure, allocating resources, or even limiting development in highly affected areas. Results from this study could contribute to the coastal communities so that they can better prepare for the associated hazards and begin to improve their resilience against this ongoing threat.

CHAPTER II

STUDY AREA

2.1 Introduction

The study region is the Coastal Bend of Texas (Figure 2). It constitutes twelve counties in total, including Jim Wells, Live Oak, Karnes, De Witt, Calhoun, Goliad, Refugio, Bee, Victoria, Nueces, San Patricio, and Aransas (Figure 2). This study can be broken down into two different categories: a regional study area, and a localized study area. The regional study area is the central Coastal Bend (Jim Wells, Live Oak, Karnes, De Witt, Calhoun, Goliad, Refugio, Bee, and Victoria counties), where deformation rates from permanent GNSS stations and InSAR were generated. The local study area consists of the coastal counties Nueces, San Patricio, and Aransas where the gravity and campaign GNSS surveys were conducted (Figure 2).

Land cover in these areas consists mainly of agricultural, water, urban, and rangeland (Figure 3). Corpus Christi proper and Victoria are developed urban areas surrounded by sprawling cultivated cropland. Alice, Beeville, Three Rivers, George West, Karnes City, Goliad, and Port Lavaca are all smaller towns. The surrounding inland areas consist mostly of rangeland, pasture, shrub, and mixed forest (Stukey et al., 2004.). North Padre Island and Port Aransas are small towns located on the barrier island, which consist of emergent herbaceous wetlands. Rockport is a small town situated on a peninsula that is characterized by deciduous forest and emergent wetlands (Dewitz 2021).

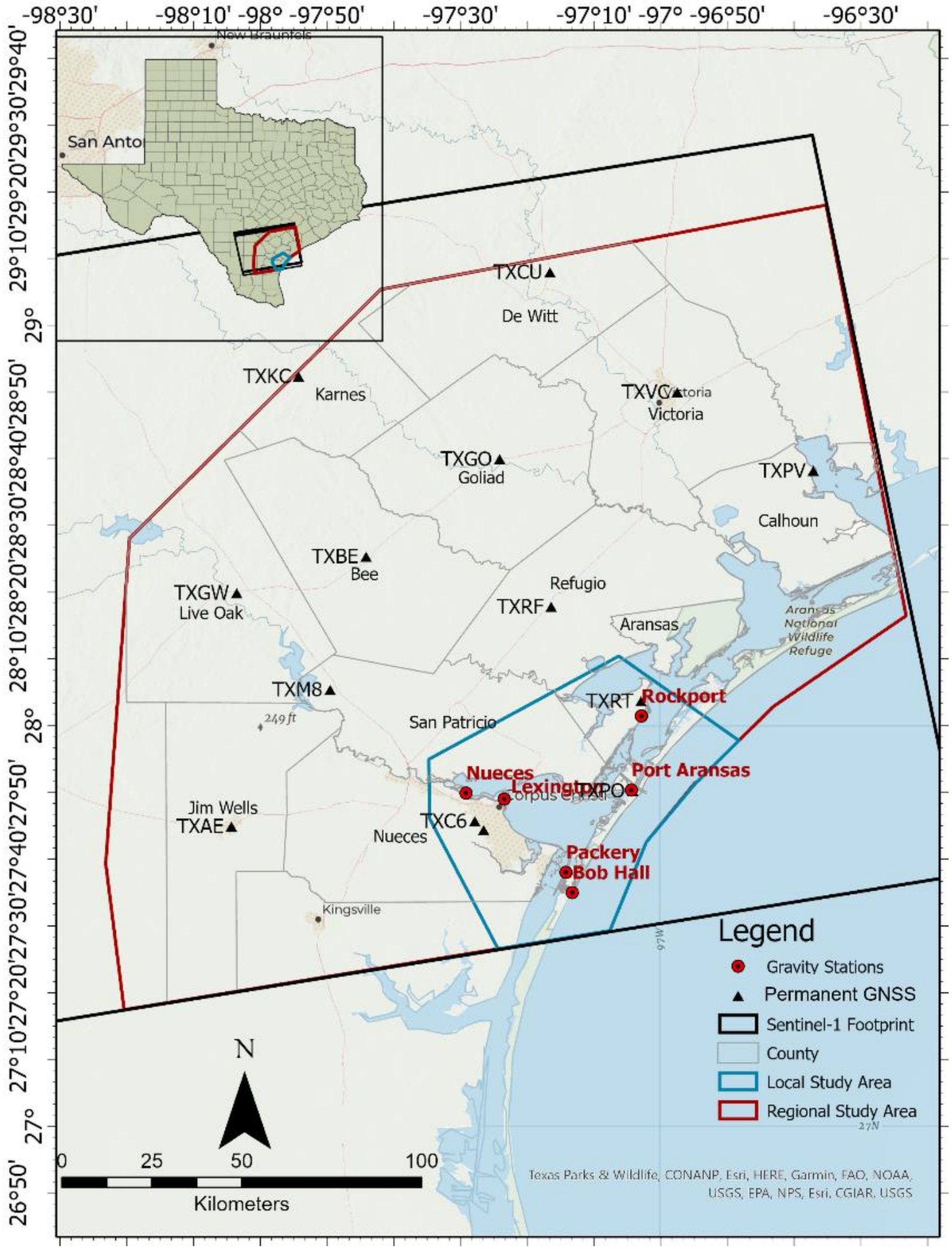

Figure 2: Regional study area (red polygon) containing permanent GNSS stations (black triangles), and local study area (blue polygon) containing gravity and campaign GNSS stations (red circles). Black polygon depicts Sentinel-1 footprint.

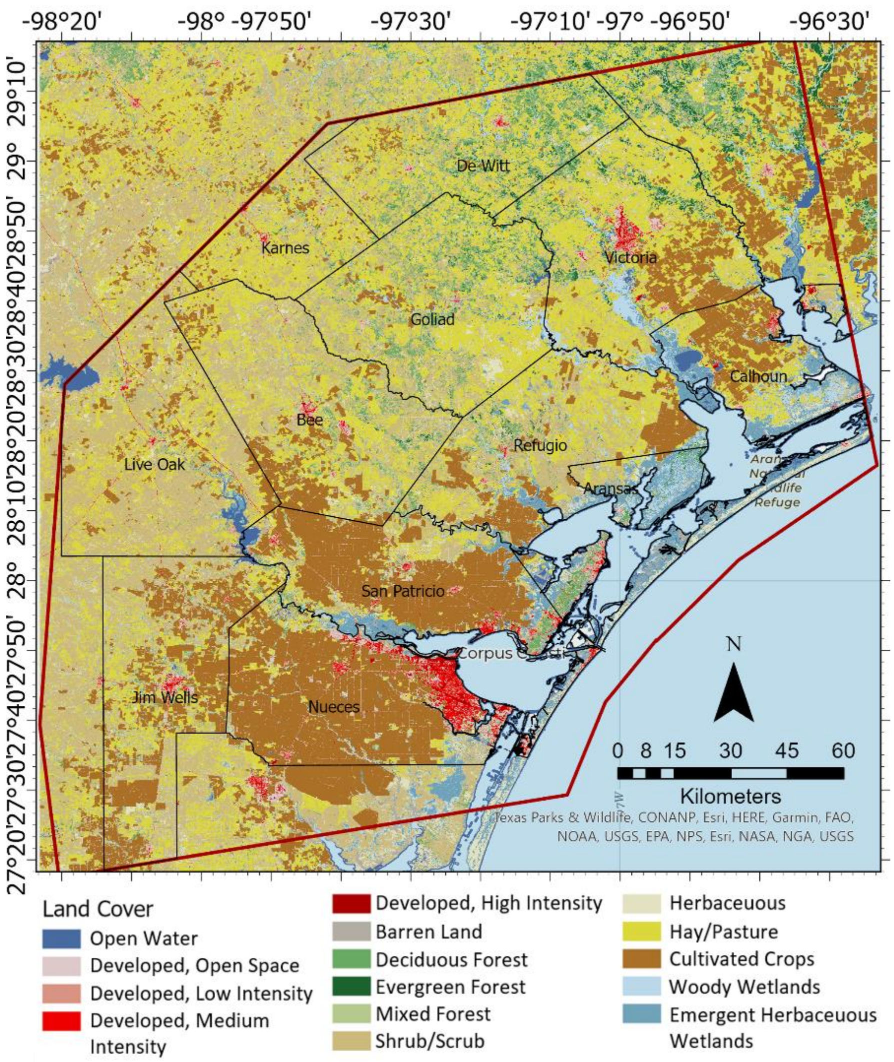

Figure 3: Land cover of the study area (Dewitz 2021).

2.2 Geologic and Hydrogeologic Settings

The study area is located on a passive depositional margin. The Coastal Bend of Texas is made up of highly compressible deltaic sediments (e.g., clay, sand) that were introduced through the fluvial system (Zhou et al. 2021) and marine deposits that consist of sand, silt, mud, and clay layers (Figure 4). The Corpus Christi and Rockport areas are underlain by the Beaumont Formation, which consists of mostly clay, silt, sand, and gravel, overlain by fine sand and scarce shell beach deposits along the shoreline. The Beaumont ranges in age from the Holocene to the Pleistocene (Stoeser et al. 2005). North Padre Island and Port Aransas, located on the barrier islands, consist of Holocene alluvium that is mostly fine-grained, well sorted sand with abundant shells and shell fragments. Silt and clay layers intergrade in the landward direction. Further inland, the Lissie Formation consists of sand, silt, and clay with minor amounts of gravel. The Willis Formation consists of clay, sand, and silt of Pliocene age. Beeville and Goliad are located in the Goliad unit, which is characterized by limestone, marl, clay, and sandstone from the Pliocene (Figure 5). George West, Live Oak, and Karnes are surrounded by the Fleming Formation and Oakville Sandstone, which are thick bedded sandstone with calcareous clay from the Miocene (Texas Water Science Center, 2014). The entire region is underlain by the Frio and Vicksburg formations, which date back to the Oligocene (Loucks 1978). Because these formations are clay and sand facies, the region is also characterized by a system of regional growth faults, which extend parallel to the coastline with fault planes dipping toward the Gulf of Mexico (Ewing et al. 1986; Hammes et al. 2004). The faults in this area form along shelf margins through sediment loading and slumping (Young et al. 2012).

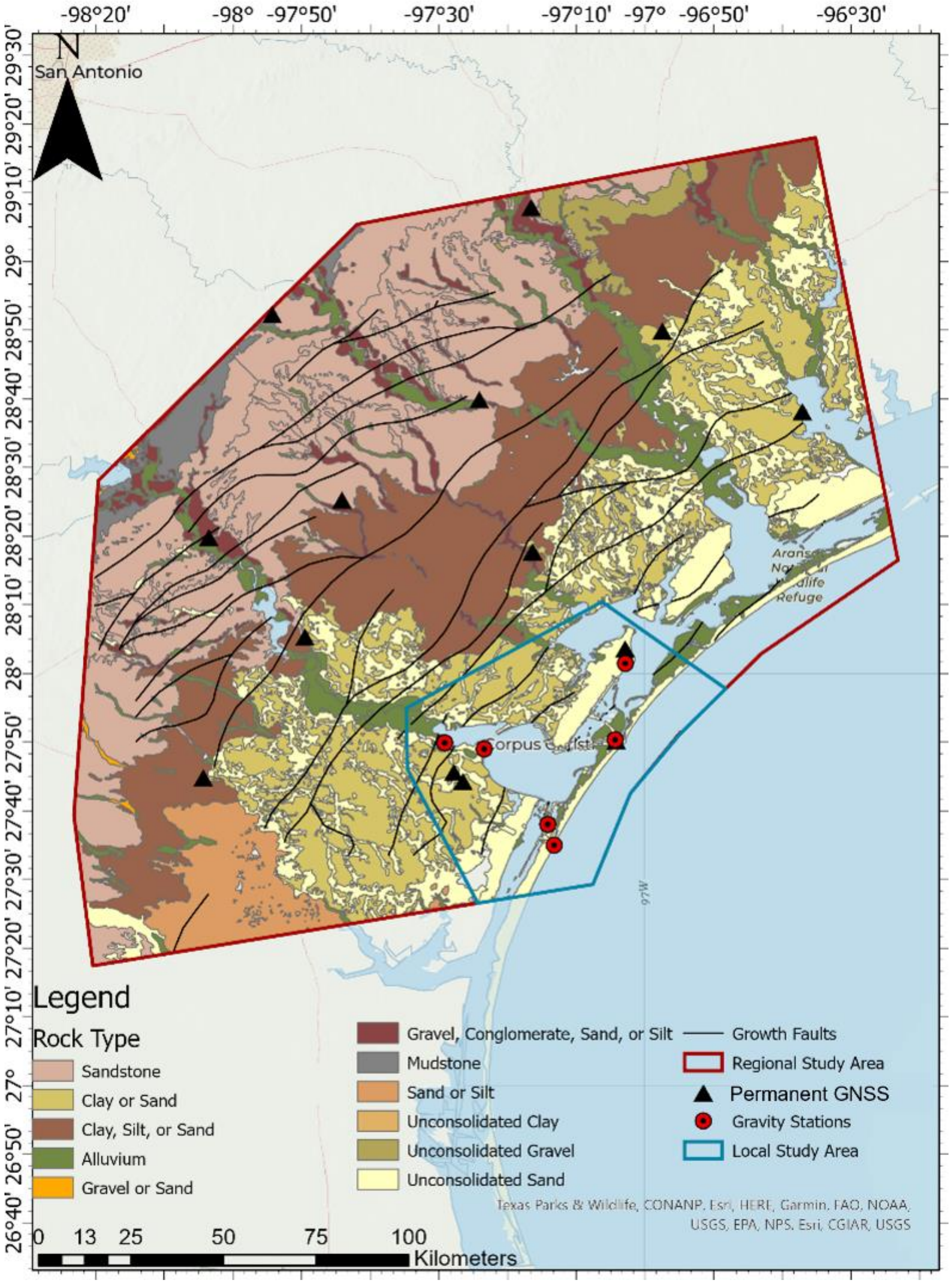

Figure 4: Surface geology of the study area (Stoeser et al. 2005) *as well as regional growth faults (black lines)* (Ewing et al. 1986; Hammes et al. 2004). *Included are the permanent GNSS stations in black triangles and gravity stations in red circles.*

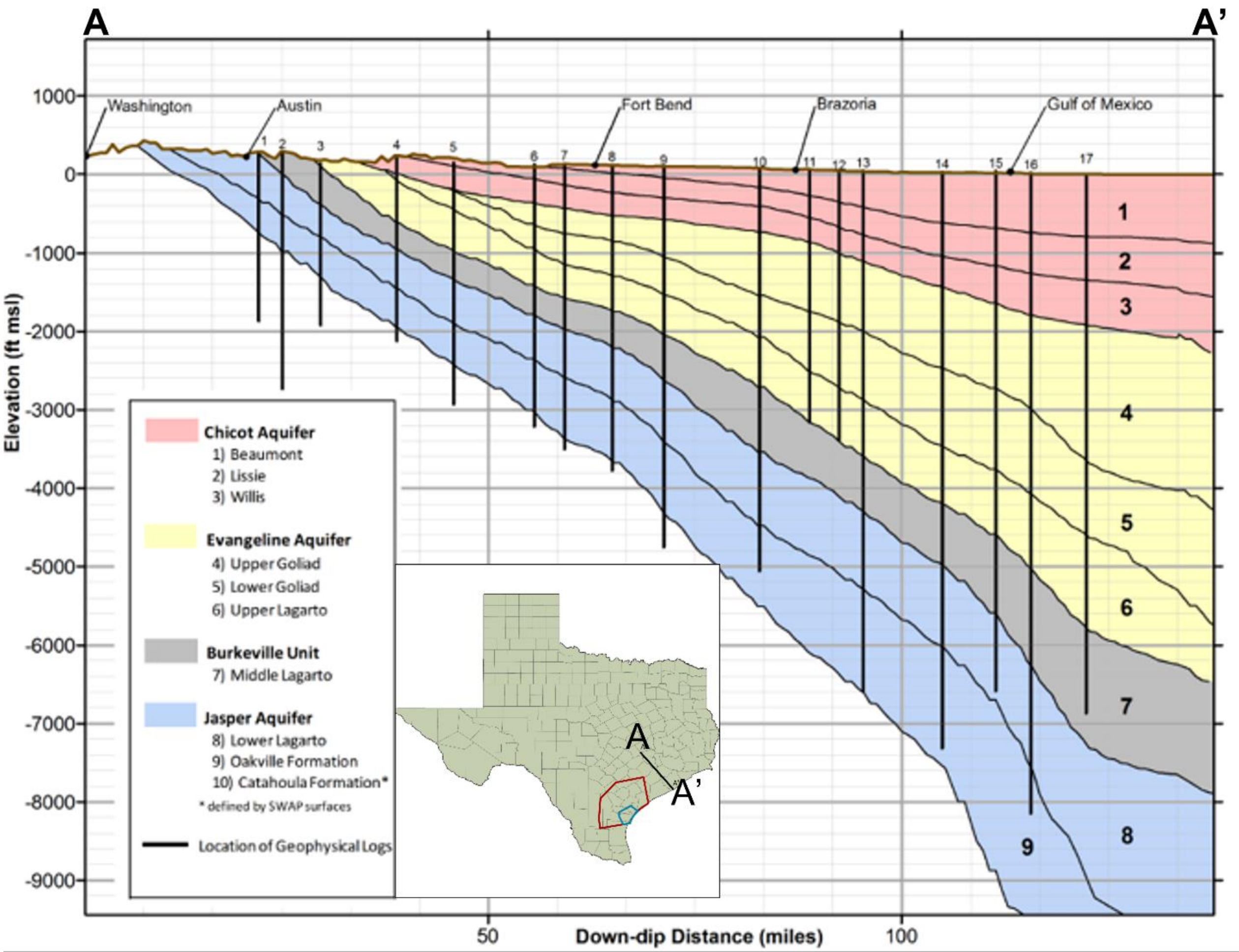

Figure 5: Subsurface geologic cross section showing the geological and major aquifer units in the study area (Young et al. 2012). *The Beaumont, Lissie, Willis, and Goliad formations are primarily clay, silt, and sand. The Lagarto, Oakville, and Catahoula are predominately sandstone. This cross section is located up the coast just north of the study area (black line on the inset map).*

The hydrogeology of the Coastal Bend is characterized by that of the Gulf Coast aquifer (GCA) system. This system consists of three main aquifers including the Jasper, Evangeline, and Chicot aquifers (Figure 5), and stretches from the Louisiana border to Mexico while running parallel to the Gulf of Mexico (Casarez 2020). The study area is situated in over the central part of the GCA, and includes the Jasper, Evangeline, and Chicot (Figure 6). The groundwater in this region flows from the west towards the Gulf of Mexico in the east (Chowdhury and Mace 2001).

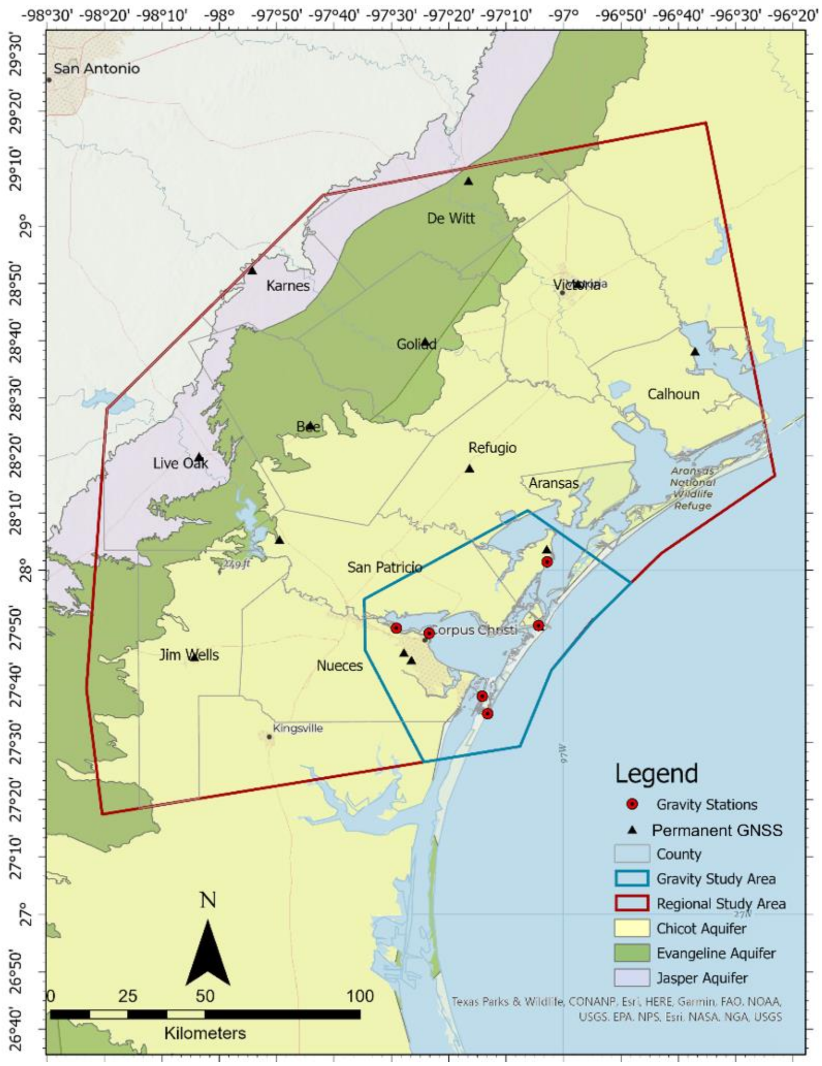

Figure 6: Aquifer units within the study area, including the Chicot, Evangeline, and Jasper aquifers. Red outline is the extent of the study area, while the red circles are the gravity stations and the black triangles are the permanent GNSS stations (Casarez 2020).

2.3 Fluid Extraction Rates

Total groundwater extraction rates within the study area are estimated to be 518×10^9 m^3 per year (Haley et al. 2022). Figure 7 shows annual average groundwater extraction rates from a historic period between 2000-2015, and the difference in rates from the current study period (2016-2022) and the historic period. County extraction rates were retrieved from Texas Water Development Board (TWDB) website (https://www.twdb.texas.gov accessed 20 September 2022). The county averaging the highest annual extraction rates (both during the historical period and the study period) was Victoria, while the county with the lowest annual extraction rates was Aransas (both during historical and study period) (Figure 7).

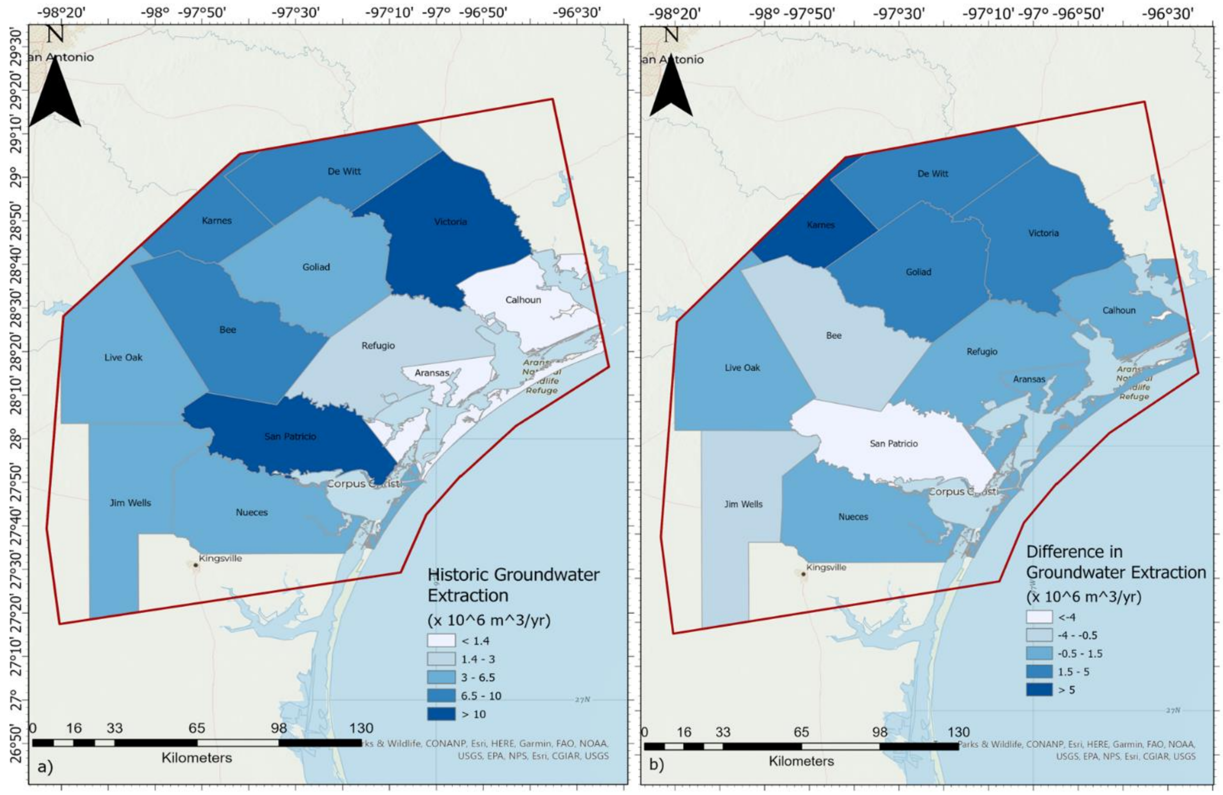

Figure 7: a) Historic average annual groundwater extraction rates by county from 2000 to 2015. b) changes in groundwater rates between 2016 to 2022 and the historic rates from 2000 to 2015.

The annual average oil and gas extraction rates were determined for each county during the historic period of 2000-2015, as well as the study period of 2016-2022. Figure 8 shows the historic rates and the difference in rates from the current study period (2016-2022) and the historic period. These rates differ significantly from county to county (Figure 8).

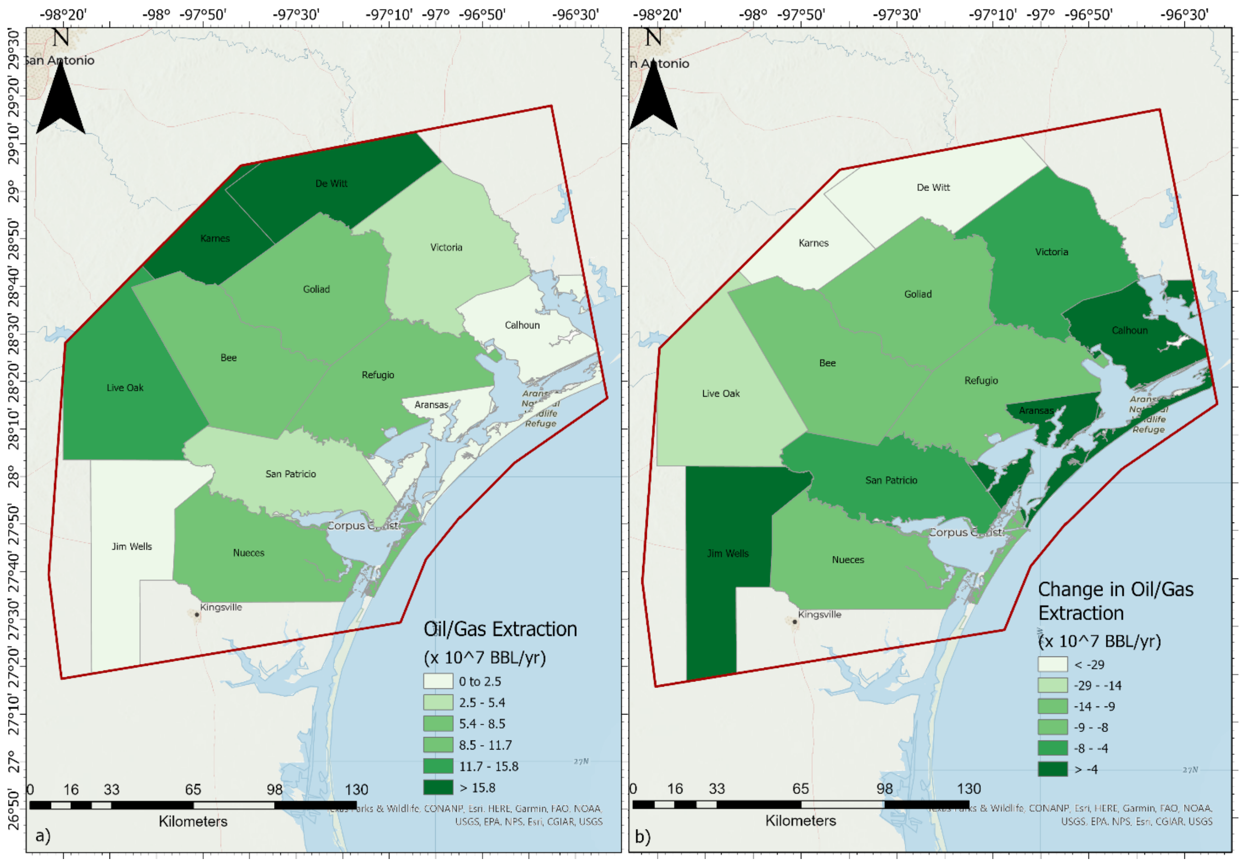

Figure 8: . a) Oil and gas extraction rates in BBL/year during the historical period 2000 to 2015 a) changes in oil/gas extraction between the study period 2016 to 2022 and the historical period.

During both the historical and current study period, Karnes remained the county with the highest average annual oil and gas extraction rates. During the historic period, Jim Wells County had the lowest average annual hydrocarbon extraction rates, and Calhoun has the lowest rates during the current study period. The oil and gas extraction rates were determined from the Texas Railroad Commission (TRC) website (https://www.rrc.state.tx.us/ accessed on 21 April 2022).

2.4 Subsidence in Coastal Texas

Over the years, several studies have been conducted along the Texas coast investigating the rates, locations, and factors controlling subsidence. These studies used a variety of datasets such as tide gauge measurements (Swanson and Thurlow 1973; Paine 1993; Letetrel et al. 2015; Liu et al. 2020; Zhou et al. 2021), GPS measurements (Bawden et al. 2012; Qu et al. 2015; Letetrel et al. 2015; Liu et al. 2020; Zhou et al. 2021; Haley et al. 2022), InSAR or satellite altimetry (Bawden et al. 2012; Qu et al. 2015; Letetrel et al. 2015; Haley et al. 2022), and core data (Simms et al. 2013; Al Mukaimi et al. 2018).

These studies determined that subsidence rates have increased over time, and that rates generally increase with proximity to shoreline and deltas (Simms et al. 2013; Zhou et al. 2021) as well as around high intensity urban areas like Houston or Galveston (Bawden et al. 2012; Qu et al. 2015). Subsidence rates along the Texas coast were determined to range from -1.4 mm/yr to -7 mm/yr (Letetrel et al. 2015; Zhou et al. 2021), while rates in the Houston-Galveston region were reportedly as high as -53 mm/yr in some areas (Qu et al. 2015). The main driving factors of subsidence along the Coastal Bend of Texas were determined to be primarily fluid extraction (groundwater and hydrocarbon) (Swanson and Thurlow 1973; Paine 1993; Simms et al. 2013; Liu et al. 2020), compaction of Holocene sediments (Simms et al. 2013; Letetrel et al. 2015; Zhou et al. 2021), and growth faulting (Qu et al. 2015; Haley et al. 2022).

Two studies specifically investigated subsidence around the central Coastal Bend, which includes the areas covered in this paper. The first was a study done along the Texas coast determined natural subsidence rates derived from GPS and tide gauge measurements from 1940's to 2020 (Zhou et al. 2021). The study detailed historical subsidence rates for Rockport and the Corpus Christi area. The tide gauge-derived results indicated that the site in Rockport experienced steady subsidence of -2.3 mm/yr from the 1940's to the 1980's, then underwent a period of rapid subsidence during the 1990's where rates indicated subsidence of -10 mm/yr. This period of rapid subsidence is thought to be due to anthropogenic groundwater withdrawals, and once groundwater regulations were enforced at the end of the century, rates slowed to around -0.8 mm/yr. Results from the Corpus Christi location indicated a steady rate of -0.8 mm/yr from 1984. According to the study, leveling surveys from earlier surveys report rapid subsidence in Corpus from 1942 to 1975 with rates of approximately -5 cm/yr. The subsidence during that period was primarily thought to be due to withdrawal of oil, gas, and groundwater. The current (2010-2020) rate of subsidence according to this study is -1.4 mm/yr along the Texas coastline, with rates in the Corpus Christi, Rockport, and Port Mansfield area ranging from -0.6 to -0.8 mm/yr. The study attributed the subsidence to natural consolidation of the Jasper, Evangeline, and Chicot aquifers (Zhou et al. 2021).

The second study specifically investigated the central Coastal Bend of Texas used InSAR calibrated against GNSS-derived rates (Haley et al. 2022). This study looked at subsidence rates during the period of October 2016 to July 2019 and found that there was ongoing subsidence in the Karnes City, Live Oak, Victoria, Refugio, and Corpus Christi areas. Subsidence rates averaged about -6.8 mm/yr across these areas, ranging from -3.5 mm/yr around the Corpus Christi Bay area, to -9.0 mm/yr in Live Oak. Subsidence in the study was attributed to fluid extraction and growth faulting (Haley et al. 2022).

CHAPTER III

DATA AND METHODS

3.1 Overview

An integrated approach was used to investigate the study objectives, consisting of four independent datasets and techniques (Figure 9). Initially, gravity and campaign GNSS surveys were undertaken to monitor land subsidence on a local scale, focusing on six key locations around Corpus Christi, the barrier islands of North Padre and Mustang, and Rockport. In order to provide a more comprehensive and regional view of land deformation around the Texas Coastal Bend, the small baseline subset (SBAS) Interferometric Synthetic Aperture Radar (InSAR) technique was utilized. The use of InSAR allows for a more widespread temporal coverage that spans from 2015 to 2021. Additionally, InSAR results were validated and constrained using permanent GNSS stations. The gravity and campaign GNSS-derived rates were compared; the InSAR and permanent GNSS rates were also compared in order to validate results. Factors controlling the rates of observed subsidence were then investigated.

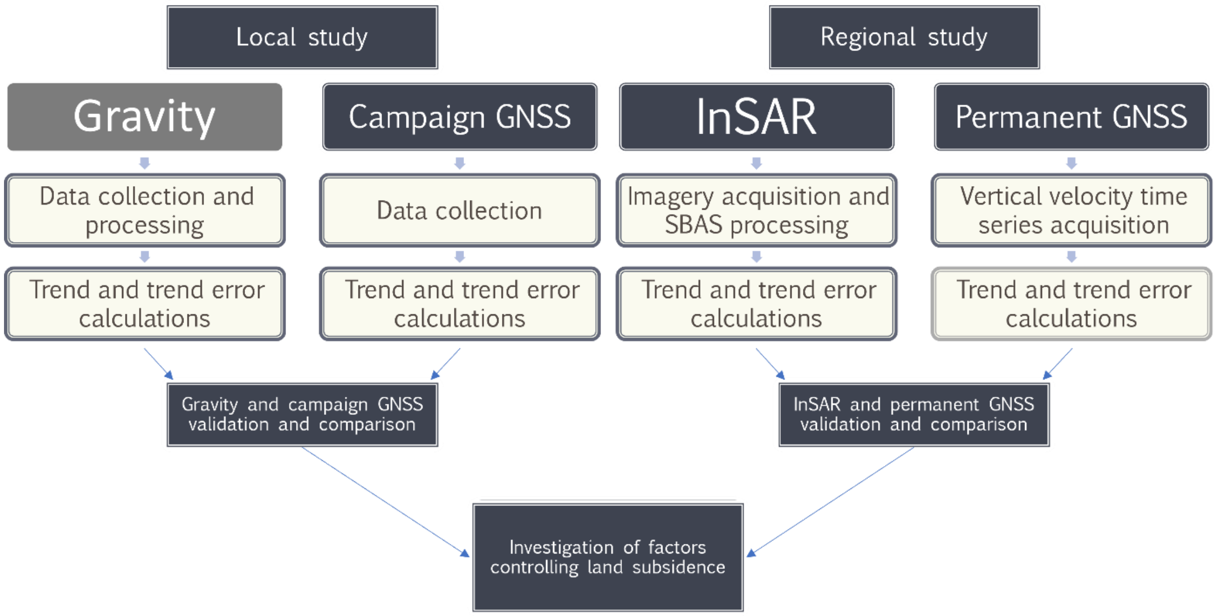

Figure 9: Methodology flowchart depicting individual datasets, steps for acquisition and processing, and overall integration for comparison and validation.

3.2 Gravimetry for Monitoring Land Subsidence

3.2.1 Gravity Surveys

A gravity survey was conducted around the Texas coastal bend. A network of six gravity stations was established with data collection taking place every two weeks (Figure 10). The survey loop began and ended at the reference base station located at Texas A&M University- Corpus Christi. The gravity stations were located at Packery Channel, Bob Hall Pier, Port Aransas, Rockport Harbor, Nueces Bay, and the Lexington. Gravity stations were chosen to ensure widespread coverage around the Corpus Christi Bay, barrier islands, and Rockport area, while also maintaining a small enough survey loop to minimize drift effect. The survey period was October 1, 2020, through September 30, 2022. Since the project's inception, 40 observations have taken place at each survey location over a 23-month period, with daily surveys lasting approximately five hours.

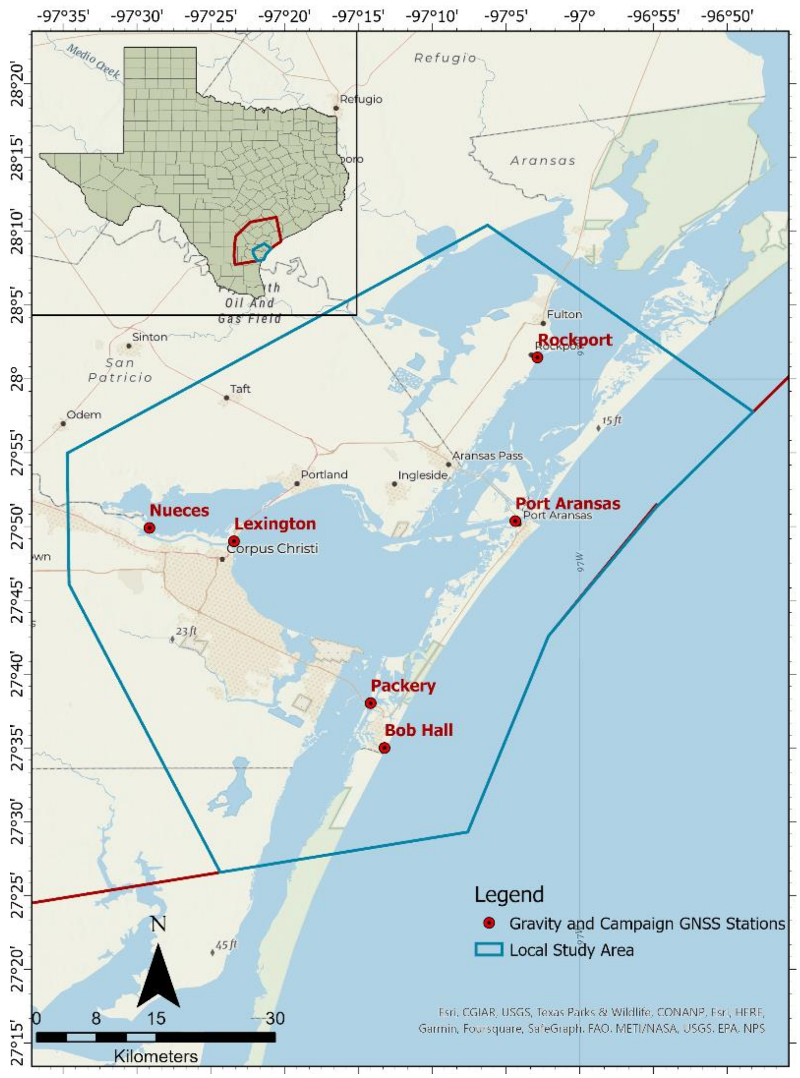

Figure 10: Local study area with gravity and campaign GNSS station locations (red).

For this study, a LaCoste & Romberg G-976 relative gravimeter (with an estimated accuracy of ± 0.01 mGal (Nakagawa et al. 1973)) was used to take three readings at each station per survey (Figure 11). This instrument involves a beam with a highly sensitive zero-length spring. A test mass is attached to the spring, which generates a counterforce to keep the mass in equilibrium with the gravitational force. The condition of equilibrium can be explained by:

$$mg = k(l - l_0) \qquad (1)$$

where *m* is mass, *g* is gravity, the spring constant is *k*, and the elongation of the spring is the spring length under load *l* and the length without load l_0. In order to determine the difference in gravity, the change in the spring length must be measured using:

$$\Delta g = \frac{k}{m}\Delta l \qquad (2)$$

where Δg is the change in gravity, and Δl is the change in the spring length (Timmen 2010).

To obtain accurate measurements, the gravimeter must be leveled using both a bubble and electronic level prior to making observations at each station. Gravity causes the mass to diverge from the horizontal position, and the position of the beam can be determined by the image of the crosshair in the microscope eyepiece of the meter. The position must be restored by turning the nulling dial, which adds or subtracts a small force, until the crosshair meets the reading line. The difference between two readings gives a dial reading, which corresponds to a gravity difference. The gravity value, expressed in units of milligals, is converted by multiplying the counter reading by the interval factor (interval factor obtained from calibration table, which is unique to each meter) (Romberg 2004). In the case of the gravimeter used for this survey, the interval factor (or dial constant) was 1.02379.

Figure 11: a) Gravity and campaign GNSS data acquisition at Port Aransas station. b) The employed LaCoste and Romberg gravimeter.

3.2.2 Gravity Precision Test

An independent experiment was conducted in order to test the precision of the gravimeter. The experiment consisted of two survey loops completed over the span of three days. Three measurements were taken at the reference base station, three at Packery channel, and then three more at the base station again. This process was repeated twice a day and data were collected for three days. Gravity values were corrected for drift and tide variations, then compared.

3.2.3 Gravity Data Processing

Spatial and temporal variations in Earth's gravitational field can be affected by oceanic and solid Earth tides. Because of this, tides must be accounted for and removed from the observed gravity data before converting them to elevations. In addition, the gravity values were corrected for drift effects.

i. Drift Corrections

The LaCoste and Romberg gravimeter is an extremely sensitive instrument that relies on the principle of an astatic pendulum. A horizontal beam is supported by a zero-length spring, which is a spring that has been prestressed so that it is above a critical tension. A fixed mass is attached to the spring. The force that the mass exerts on the spring varies between each station with the local gravitational acceleration, and over time, changes occur in the gravimeter spring due to elastic creep. Drift can be caused by factors such as environmental factors such as changes in pressure and temperature, transportation between stations, and any kind of jostling or shock that may occur during routine handling. Drift should be accounted for with every survey loop by obtaining a base station reading at the beginning and end of the survey, forming a closed loop that can be used to calculate a drift coefficient. The drift effect is explained as:

$$\Delta\hat{L}_{ij} = \Delta L_{ij} + v_{ij} = \left(g_j - g_i\right) - D(t_j - t_i) \qquad (3)$$

where $\Delta\hat{L}_{ij}$ is the raw gravity difference, ΔL_{ij} is the drift-corrected gravity difference, v_{ij} is the residual, g_i and g_j are initial and final gravity values, D is the drift coefficient, and t_i and t_j are initial and final times of measurement (Hwang et al. 2002).

ii. Tide Corrections

The gravitational pull of the Sun and Moon on the ocean causes cyclic variations in sea level. Additionally, the “solid” Earth also responds to the time varying gravitational acceleration due to the motion of the Sun and Moon. Solid earth tide is measured by satellite or gravimeters, and it consists of two components: the direct upward pull of the sun and moon, and the decrease in gravity as the earth’s surface is pulled further from the center of the earth (Wahr 1995) . As such, a multiplicative term (Elastic Response factor) must be taken into account when correcting for tidal effects in consideration of the non-rigidity of earth. Tide was corrected for by using a technique advanced by Longman (Longman 1959). This technique uses formulas that express tidal acceleration in terms of zenith angle and the distance of the earth, sun, or moon, and then develops the solar and lunar tides into harmonic constituents (Longman 1959). This allows for tidal acceleration to be computed at any point on earth at any given time.

For this study, the solar and lunar tidal effects was determined for each station at the minute the gravity readings were taken and then corrected using GravTide software, which uses an Elastic Response factor of -1.2 to calculate the effect of non-rigidity.

iii. Trend and Trend Error Calculations

Once the aforementioned corrections were applied to the raw gravity measurements, trend calculations needed to be performed. This was done by fitting a linear regression model to determine the slope of the gravity values over time as well as the change in gravity-derived height over time. The slope uncertainty was then calculated using the following equation:

$$\sigma_m = m\sqrt{\frac{1/R^2-1}{n-2}} \qquad (4)$$

where σ_m is the uncertainty of the slope, R^2 is the coefficient of determination, n is the number of data points, m is the slope, and (Ross 2010). Significance levels of the calculated trends were also calculated.

iv. Gravity to Height Conversion

In this study, gravity trends were then divided by the admittance factor of -0.3086 to obtain a rate representative of the change in height per year according to this equation:

$$H = \frac{\Delta g}{C} \qquad (5)$$

where H is height, Δg is the change in gravity from each reading's deviation from the initial station's reading, and C is the admittance factor (Torge 1986). The admittance factor accounts for changes in gravitational acceleration due to the elevation at which the measurement was made

(Torge 1986; Hwang et al. 2010). Use of this admittance factor implies that change in gravity is due to consolidation of soil, and not change in mass.

v. Temporal Variability Calculations

In order to quantify temporal variability in measurements, the proportional variability index PV was determined for each time series generated. The PV determines the average proportional variability among every combination of values in a time series to assess variability (Fernández-Martínez et al. 2018). This makes it effective for analyzing temporal variability. PV can be expressed by with the following equation:

$$PV = \frac{2\sum z}{n(n-1)} \qquad (6)$$

where n is the number of values in a variable, and z is the list of individual values. A low PV represents stability, while a higher PV indicates differences between abundances (Heath 2006).

3.3 Campaign GNSS Survey

The Trimble R8S Integrated GNSS System was used to conduct a GNSS real time kinematics (RTK) measurement campaign alongside the gravity survey (Figure 10). High-precision survey position measurements were collected using a virtual reference station (VRS) technique. The VRS is an imaginary, unoccupied reference station which is only a few meters from the RTK user. For this position, observation data are created from the data of surrounding reference stations as though they had been observed on that position by a GPS receiver (Landau et al. 2002). The campaign GNSS measurements were collected every two weeks, and the elevation values were then used to derive a displacement trend to compare against the gravity results. Trend and trend error calculations were carried out by fitting a linear regression model and determining the slope of the changes in elevation over time. Additionally, trend errors and significance were calculated following the same steps described in Section 3.2.3.iii “Trend and Trend Error

Calculation", and temporal variability was calculated using the equation in Section 3.2.3.v "Temporal Variability Calculations".

3.4 Remote Sensing to Detect Land Subsidence

3.4.1 SAR Dataset

In this study, SAR images were used to detect and quantify land deformation in the study area. SAR provides high-resolution two-dimensional images that can monitor the active processes on the surface of the Earth (Moreira et al. 2013). SAR systems transmit electromagnetic pulses in different bands, and when the pulse interacts with the surface of the earth, the system antenna receives a backscatter signal. The attributes of the backscattered signal, such as the amplitude and phase, depend on the physical properties of the target object (Walker et al. 2004). Depending on the frequency band used by the sensor, these signals can penetrate vegetation, snow and ice, cloud cover, and even dry soil. As such, SAR systems allow imaging to be done during day, night, and a variety of other conditions (Moreira et al. 2013). The table below depicts commonly used frequency bands, their corresponding wavelengths, and most frequently used applications (Table 1).

Table 1: Most frequently microwave bands used in SAR sensors, with frequency, wavelength, and the common applications (modified from website https://www.earthdata.nasa.gov/).

Band	Frequency	Wavelength	Common Application
X	8–12 GHz	3.8–2.4 cm	High resolution SAR (urban monitoring,; ice and snow, little penetration into vegetation cover; fast coherence decay in vegetated areas)
C	4–8 GHz	7.5–3.8 cm	SAR Workhorse (global mapping; change detection; monitoring of areas with low to moderate penetration; higher coherence); ice, ocean maritime navigation
S	2–4 GHz	15–7.5 cm	Little but increasing use for SAR-based Earth observation; agriculture monitoring
L	1–2 GHz	30–15 cm	Medium resolution SAR (geophysical monitoring; biomass and vegetation mapping; high penetration, InSAR)
P	0.3–1 GHz	100–30 cm	Biomass, vegetation mapping and assessment.

SAR is an aerial, unmanned aerial vehicle (UAV), or spaceborne system that consists of a side-looking radar. As the system moves along a path or azimuth direction at a certain altitude, it emits short microwave pulses through the antenna attached to the platform to the Earth, and then receives the electromagnetic signals as they reflect. This creates an antenna footprint, or ground range extent of the scene the pulse covers, in the range direction perpendicular to the azimuth direction (Moreira et al. 2013).

The amplitude and phase of backscatter is recorded by the sensor. Amplitude describes the return signal strength, and the phase measures the relative sensor to target distance. Depending on the physical and electric properties of the target surface as well as the radar system properties, the strength of the backscattered signal varies (Walker et al. 2004; Moreira et al. 2013).

In order to quantify the rates of subsidence, this study utilized 127 Interferometric Wide swath (IW) mode Single Look Complex (SLC) SAR imagery acquired from the Sentinel-1 mission from January 2017 to November 2021 (Table 2). Sentinel-1 is a two-satellite constellation that carries a C-band (5.6 cm wavelength) SAR instrument. It is a joint mission between the European Commission (EC) and the European Space Agency (ESA). The Sentinel-1 mission provides spatial resolution of 20 meters with a ground range resolution of 5 meters, and a temporal resolution of 6 – 12 days (Space Agency 2012). The images, downloaded from the Alaska Satellite Facility (ASF) SAR Distributed Active Archive Center (DAAC) run by the National Aeronautics and Space Administration (NASA), were acquired along the ascending flight track 107 frame 88 (https://asf.alaska.edu/).

Table 2: Details of Sentine-1 scenes used to observe surface deformation in this study.

SAR Instrument	Orbit Type	Track	Frame	No. of Images	Normal Baseline		Temporal Baseline		Start Date	End Date
					Mean	Max	Mean	Max		
Sentinel-1	Ascending	107	88	127	43	135	48	84	Jan-17	Nov-22

3.4.2 InSAR

Visualizing raw SAR imagery does not inherently give useful information about the target area in terms of quantifying deformation processes, however, SAR interferometry (InSAR) uses two or more SAR images to detect patterns of deformation, subtle changes in elevation, and extract landscape topography (Figure 12) (Lu et al., 2007.). This capability makes it a powerful tool for constructing digital elevation models (DEM), imaging earthquake displacement such as co-seismic and post-seismic deformation of surface faults, mapping deformation from volcano dynamics, monitoring slope instability for landslide displacements, mapping water level changes in wetland areas, and, as in this study, surface displacement due to land subsidence (Lu et al., 2007; Prati et al., 2010). The InSAR technique has high accuracy and can detect these displacement processes at a spatial resolution of tens-of-meters (Lu et al. 2007).

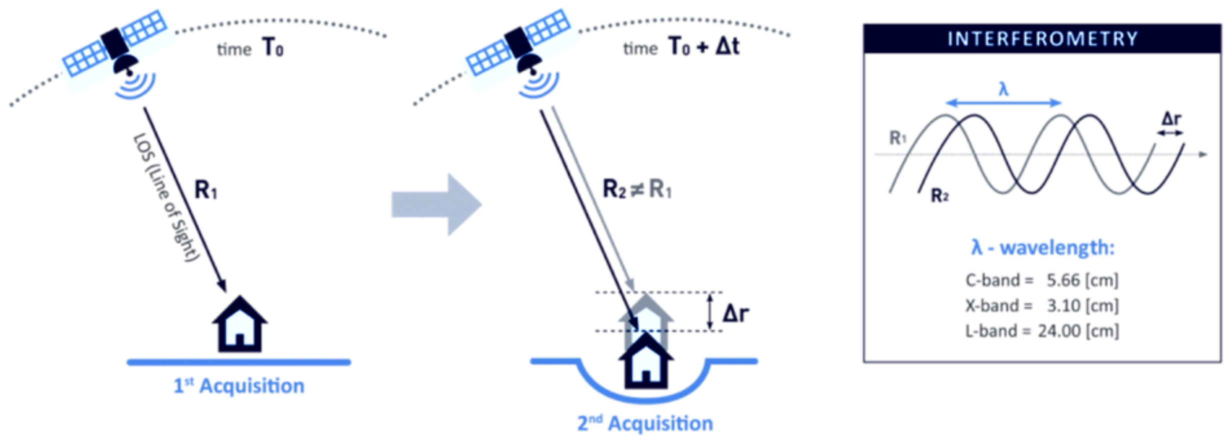

Figure 12: Two SAR images of the same place at different times (T0 and T0 + ΔT) give two distances to the ground (R1 and R2). The phase difference between these two distances shows ground deformation.

The interferometric phase consists of six components: the phase noise component, the displacement component, the topographic component, the orbital component, the scatter component, and the atmosphere component (Equation 7). InSAR combines the phase information from two spatially or temporally separated antennas to assess the difference between the sensors and target surface. When the SAR images of the same area are acquired over different times are co-registered, the electromagnetic waves interfere, or interact in a way that either combines to intensify the waves or cancels them out. The difference is calculated between their corresponding phase values, and the resulting InSAR image, or interferogram, displays these interferences as a series of patterns or fringes. Phase changes can be due to landscape topography, surface deformation, noise (systematic or environmental), orbital variability between acquisition times, or delays in atmospheric propagation (Lu et al., 2007). The similarity of the co-registered SAR images is measured to calculate the ratio between coherent and incoherent summations resulting from noise, spatial decorrelation, and scene decorrelation between acquisitions (Zebker and Villasenor 1992). Coherence ranges from 0 to 1, and the value measures the quality of the interferogram. The value decreases with the increase of noise, vegetation, and spatial and temporal baselines.

Differential InSAR (DInSAR) technique includes a processing regime that follows the following procedure (Okeke & Nguyen Ba, 2006):

Data Pre-Processing- includes data download and input, setting preferences, data cropping through sample selection, over sampling in range and azimuth direction, and orbit data download for computation of precise orbit.

Co-Registration- required when a region is covered by multiple SAR images and those images must be compared and resampled in order to align them for phase differencing. This step ensures that the pixels in the images are aligned to represent similar points on the target surface.

Interferogram Generation- generates coherence images and complex interferograms by cross multiplying the master and conjugate slave image. The interferogram contains the product of the amplitudes and difference in phase values between the images. The phase difference can reveal information about topography and deformation. Interferometric phase observation is generated according to the following equation:

$$\varphi_{int} = \varphi_{topo} + \varphi_{defo} + \varphi_{orb} + \varphi_{atm} + \varphi_{scat} + \varphi_{noise} \qquad (7)$$

where φ_{int} is interferometric phase, φ_{topo} is topographic phase, φ_{defo} is deformation phase, φ_{orb} is the orbit, φ_{atm} is the atmospheric phase, φ_{scat} is temporal and spatial phase change in scatter characteristics, and φ_{noise} is phase degradation factors (Aly et al. 2009; Crosetto et al. 2016).

Phase Unwrapping- ideally, an interferogram phase can only be modulo 2π, however, due to noise, discontinuities, and under-sampling, it is possible for phase steps to fall outside this interval. This step works to reconstruct the original phase by restoring the multiple of 2π to each pixel of the interferometric phase image (Mario Costantini, 1998; Wegmüller et al., 2002).

Geocoding- transforms an image from slant range projection to a geographic coordinate system so that products can be displayed in shape and/or raster formats for further analysis and integration with other datasets.

3.4.3 Small Baseline Subset (SBAS)

Small Baseline Subset (SBAS), an approach proposed by Berardino *et al*. (2002), is a processing technique based off the DInSAR technique that can be used to detect surface deformation and to monitor the temporal evolution of the displacement (Figure 13). It is precise to about 1-2 mm/year, a precision that decreases directly with coherence, which makes it ideal for quantifying slow rates, such as, in the case of this study, land subsidence. The SBAS technique generates a deformation time-series solved through the inversion of a specific combination of differential interferograms to produce data pairs that are categorized by small orbital separation and small temporal baselines. The process utilizes a singular value decomposition inversion to produce average surface deformation velocity, residual topography, and temporal evolution of the deformation (Berardino et al. 2002; Lanari et al. 2007; 2021).

The SBAS approach works to limit phase noise, topography errors, and spatial and temporal decorrelation effects. The method uses multilooked interferograms to generate pairs that are selected specifically in order to minimize separation baselines between acquisition orbits. This allows average displacement velocity models as well as displacement time series to be obtained for the target area (Lanari et al. 2007).

For this study, the SAR data was processed within the SARscape commercial software package, which is an ENVI module that uses the Slant Look Complex (SLC) data to generate interferograms using the SBAS procedure. The process follows a workflow that is depicted as follows:

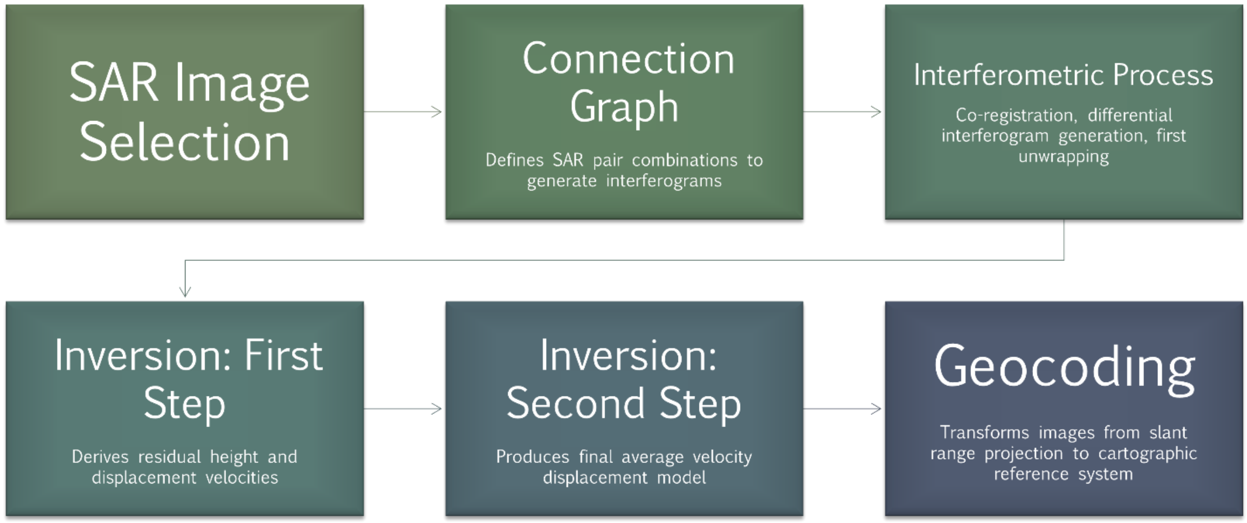

Figure 13: Workflow for the SBAS module.

The first step of the SARscape SBAS workflow is the Connection Graph generation. This step defines SAR pair combinations that will be used to generate the differential interferograms that will later be used to determine displacement related parameters. The connection network was created using 127 Sentinel-1 images spanning a six-year period (2015-2021) (Figure 14). The maximum percentage used for the normal baseline was 2%, and the maximum threshold for the temporal baseline was 90 days. The software automatically selected a super reference image (reference date September 29, 2019) against which all slant range pairs are to be co-registered.

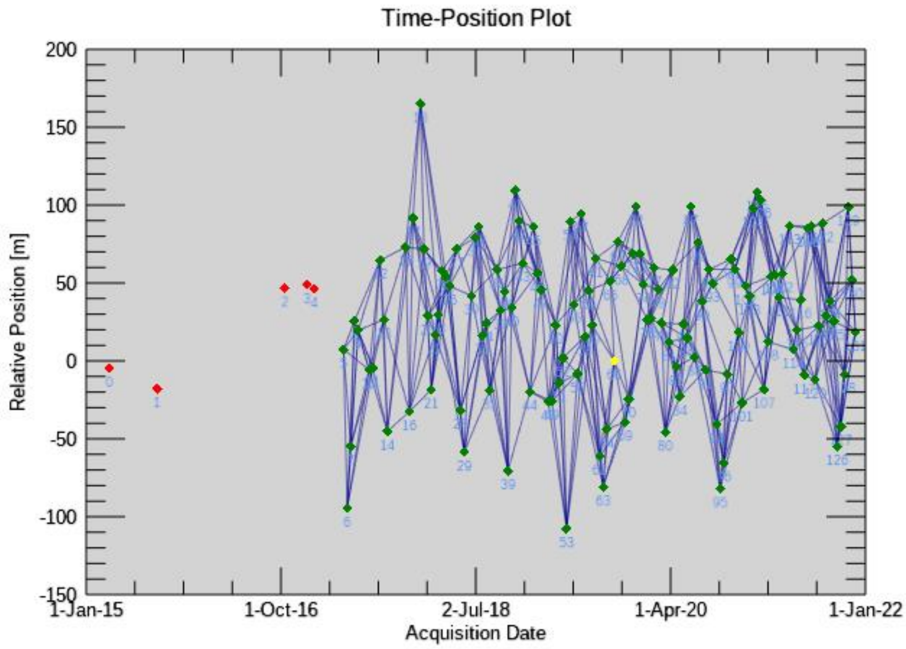

Figure 14: SBAS connection graph time-position plot generated from 127 Sentinel-1 images, with the green dots representing each image, the yellow dot signifying the super reference image, and the red dots signifying images that did not meet the normal/temporal baseline threshold criteria set.

The second step in the SBAS workflow is the Interferometric Process, in which the interferograms are generated. This process consists of three phases: Phase I, interferogram generation and flattening; Phase II, adaptive filter and coherence generation; Phase III, phase unwrapping. During Phase I, a reference DEM is utilized, and co-registration is performed to produce flattened interferograms in which the constant and topographic phases have been removed. Phase II reduces phase noise by filtering the flattened interferograms. This phase generates a master intensity filtered image, and coherence values are calculated for the interferograms. A coherence threshold of 0.3 was set for this processing step. After the filtering, Phase III can begin, and the unwrapping procedure can follow. Interferogram phase can only be modulo 2π, and once the phase becomes larger than that, the phase must start again, and the cycle repeats itself. The process involved with Phase III works to resolve this ambiguity so that the absolute phase values can be obtained (Guarnieri et al. 2003; 2021).

Once the interferograms are generated, the coherence, unwrapped, and flattened/filtered files must be inspected in order to determine which pairs should be kept or discarded from the interferometric stack. Observing the interferograms can reveal anomalies related to inaccurate phase ramps, coherence issues, effects from residual topography, and atmospheric artifacts. Once problematic interferometric pairs are removed, the SBAS process can continue.

The third step in the SBAS workflow is Inversion: First Step. Refinement and re-flattening are performed at the beginning of this step, and residual height and displacement velocities are derived with respect to the reference DEM. These modeled rates are used to flatten and redo the phase unwrapping to remove residual topography signals and improve the overall quality of the stack.

The fourth step, Inversion: Second Step, utilizes the unwrapped products derived from the previous step to determine the date-by-date displacements. Atmospheric filtering is then performed to remove the contribution of atmospheric phase components. This step produces a final average velocity displacement model.

The fifth and final step of the SBAS method is the Geocoding step. This step transforms the images from slant range projection to a cartographic reference system, and a final re-flattening is performed so that the final measurements can be associated to the defined reference points. This step generates raster and shapefiles that can be used for analysis and integration with other datasets. Displacement rates are displayed as positive or negative values, where positive is indicative of uplift and negative implies subsidence. For this study, the displacement and velocity products were projected in the vertical direction during the geocoding step. InSAR-derived rates were then calibrated by determining a relatively stable permanent GNSS station (TXCC), extracting the InSAR-derived velocity from points within a 10 m radius of the stable permanent GNSS station, determining the difference between the permanent GNSS-derived velocity and the InSAR-derived velocity, then subtracting that difference from all InSAR-derived velocities. Temporal variability was calculated for areas of displacement using the equation in Section 3.2.3 “Temporal Variability Calculations”.

3.5 Permanent Global Navigation Satellite System (GNSS) Data

Permanent GNSS stations, operated by the National Oceanic and Atmospheric Administration (NOAA), the National Geodetic Survey (NGS), and Texas Department of Transportation (TxDOT), are permanent installations that continuously measure displacement rates. Historically, permanent GNSS data have been exploited to observe the behavior of terrain movement by using satellite-based constellation systems (Psimoulis et al. 2007; Farolfi et al. 2019). While these stations are incredibly useful, their application is spatially limited to observing deformation processes at a local scale.

Over 750 permanent GNSS stations have been installed in the Gulf of Mexico region, and over 350 of them have long term observations dating back to the early 1990’s (Yu and Wang 2016). In this study, fifteen permanent GNSS stations within the regional and local study area were utilized to validate SBAS derived deformation rates (Figure 15). The length of the observation periods of these stations differ from location to location, with one of the station’s (TXCC) record length going back to 1996. The majority of stations, however, were established between 2010-2014. All stations’ displacement rates were obtained over the time period of the study, so time series in this research start in January 2017 (except in the case of the few stations that were established later than 2017, such as stations TXM8, TXRF, and TXRT, which have been active for only around two years).These displacement rates were obtained through the Nevada Geodetic Laboratory MAGNET GPS virtual platform (Blewitt et al. 2018). The stations were selected based on their proximity to regions where SBAS derived surface deformation was most prominently observed. Additionally, the stations in Corpus Christi, Port Aransas, and Rockport were selected based on their proximity to the gravity stations (Figure 15). For each station, time series plots are provided for 24 hour sample rate solutions in IGS14 reference frame (Blewitt et al. 2018).

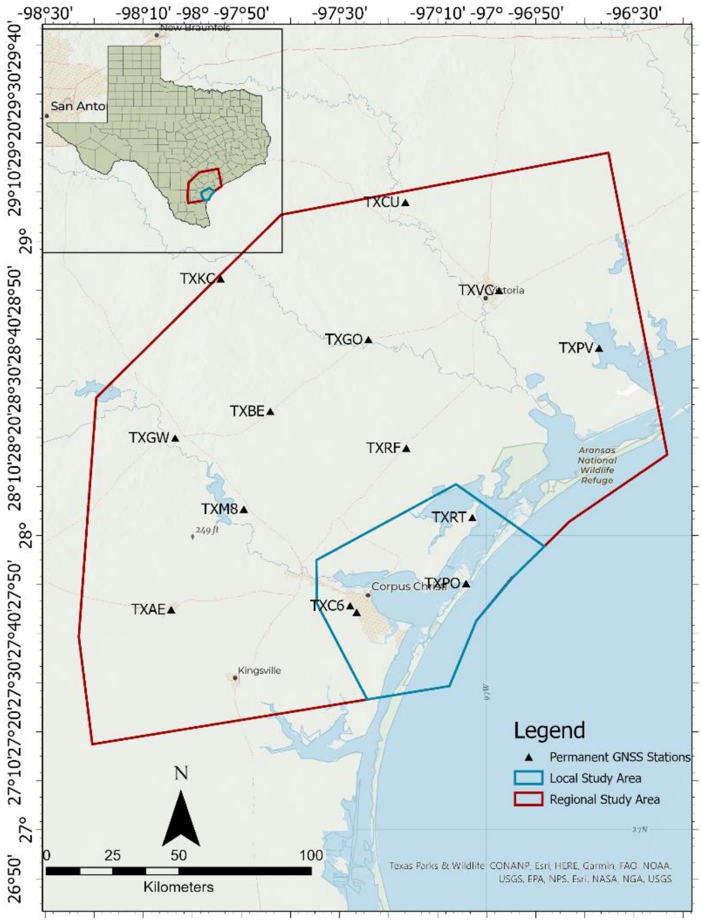

Figure 15: Regional study area displaying locations of the 15 permanent GNSS stations used in this study.

Once the appropriate permanent GNSS stations were chosen for the study, trend calculations were performed to determine changes in vertical displacement over the study time period. This was done by fitting a linear regression model to determine trend data. Uncertainty of the velocity trends derived from the stations was calculated using a 95% confidence interval (CI) methodology provided by Wang (Wang and Asce 2021):

$$95\%\ CI = 5.2\ \frac{1}{T^{1.25}} \qquad (8)$$

where the T is the year range of the time series. Temporal variability was calculated using the steps described in Section 3.2.3 “Temporal Variability Calculations”.

3.6 Data Integration

An integrated approach was used to compare and validate the individual datasets. Once the trends were determined and trend uncertainties were calculated, the values from each dataset could be compared against the trends derived from the other techniques. The individual datasets were correlated to each other based on the following parameters: regional or local scale; availability of data; similar time periods of data acquisition; proximity to nearest data points from other datasets.

The regional study includes correlation between the InSAR and permanent GNSS results, because InSAR velocities were able to be extracted over the same locations of the permanent GNSS stations. Additionally, InSAR and permanent GNSS share the same acquisition period. The regional study does not include correlation of InSAR and permanent GNSS to gravity or campaign GNSS results because the stations at which the gravity and campaign GNSS results were attained are both spatially and temporally distanced. That is, the study period for InSAR and permanent GNSS results are from January 2017 to November 2021, while the gravity and campaign GNSS study only took place from October 2020 to September 2022. Additionally, there are only six gravity and campaign GNSS stations, and they are located along the coast, and InSAR velocities were not available over two of the gravity stations (Packery and Bob Hall).

3.6.1 Local Study

Gravity-derived velocities were compared to campaign GNSS-derived velocities, as the two surveys were completed in the same locations over the same time period of October 2020 to

September 2022. This comparison was done by comparing the linear trends and calculating a correlation coefficient for the two deformation rates.

3.6.2 Regional Study

Though InSAR is a useful tool for monitoring and quantifying surface deformation, it is not without fault, and is prone to a variety of residual errors stemming from many sources. Even though the displacements and velocity products are projected in the vertical direction during the final SBAS processing step, calibrating InSAR products with other geodetic techniques can help to validate and improve the accuracy of the results. InSAR-derived velocities were compared to the permanent GNSS-derived velocities over the period of January 2017 to November 2021. InSAR-derived velocity from points within a 150 m radius of the other GNSS stations were averaged. A correlation coefficient (R) was then calculated for comparison of the deformation rates.

3.7 Factors Controlling Land Subsidence

The driving factors of subsidence were investigated and explained in this study. This was done by comparing the observed InSAR-derived subsidence rates to fluid extraction rates, groundwater levels, regional fault density, geology, and surface changes over time from historic Google Earth images.

Historic fluid extraction rates for groundwater and oil/gas were retrieved from 2000-2015. Extraction rates during the current study period were retrieved from 2015-2022. The historic rates were then subtracted from the current rates to determine the difference in extraction rates from historic rates. This difference was then compared to observed subsidence.

Groundwater levels were investigated in the areas experiencing subsidence from 2017 to 2022. This was done by extracting depth to water table data from seven groundwater monitoring wells located in or near the subsiding areas and comparing the change in groundwater to both county groundwater extraction rates as well as subsidence rates. Groundwater levels from monitoring wells data were extracted from the Texas Water Development Board (http://www.twdb.texas.gov/groundwater/data/gwdbrpt.asp) and the National Ground-water Monitoring Network (NGWMN) (https://cida.usgs.gov/ngwmn/index.jsp).

Subsiding locations were compared to their proximity to regional growth faults and the underlying geology in the area. This was done by investigating growth fault density as well as geology that characterizes the study area.

Lastly, historic Google Earth images were extracted to investigate temporal land surface changes that might control land subsidence rates. This was done by retrieving Google Earth images in seven areas experiencing enhanced rates of subsidence from 2017 and 2022 and comparing them to the InSAR-derived changes in velocity over that time period.

CHAPTER IV

RESULTS

4.1 Overview

This chapter will focus on examining the rates and locations of land deformation derived from the gravity survey, the SBAS procedure, the permanent GNSS stations, and the campaign GNSS survey. Additionally, a comprehensive comparison between results obtained from these techniques was also provided.

4.2 Land Subsidence Rates and Locations

4.2.1 Land Subsidence Derived from Gravity Survey

Results from the independent gravity precision experiment conducted over three days from April 29 - May 4, 2021 are shown in Figure 16. Examination of Figure 16 showed high precision for the employed gravimeter, with 979126.53± 0.3 mGal for the first day, 979126.58 ± 0.01 mGal for the second, and 979126.44 ± 0.2 mGal for the third and final day (Figure 16). The standard deviation for the three days was ranging between 0.01 and 0.3 mGal. These numbers were attained by averaging the six observed gravity values and determining the standard deviation for each day.

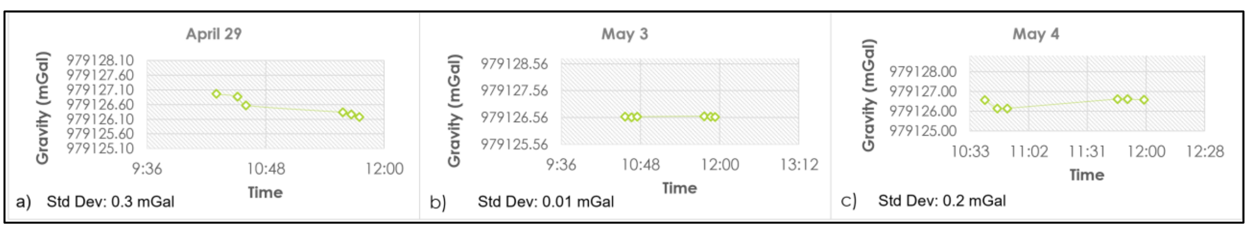

Figure 16: Results of the gravimeter precision test. (a) Results for the first day with a standard deviation of 0.3 mGal, (b) Results from the second day with standard deviation of 0.01 mGal, and (c) third day results with standard deviation of 0.2 mGal.

Figure 17 shows the spatial distribution in gravity (green) and gravity-derived height (blue) trends extracted, over the local study area, from October 2020 to September 2022. Changes in gravity measurements were in the range of -0.09 ± 0.03 mGal/yr (Lexington) to 0.03 ± 0.05 mGal/yr (Packery), with trends ranging in significance from 0.8 at Bob Hall to 0.003 at

Lexington. Lexington and Nueces, the furthest inland stations, were the only significant stations (Nueces significant at 0.04). The examined locations are also experiencing temporal variability in the measured gravity values (Figure 18). The maximum variability is shown in Rockport, with a proportional variability index (*PV*) of 1.9 x 10^{-7}, whereas Lexington (*PV* = 1.3 x 10^{-7}) displayed no little to no variability.

Examination of gravity-derived deformation rates reveal that land deformation values varied both spatially and temporally. The average rate of gravity-derived deformation rate over the study area was 103 ± 153 mm/yr. The stations (relatively) further inland displayed higher rates of uplift than those located on the near or on the barrier islands saw trends less dramatic trends.

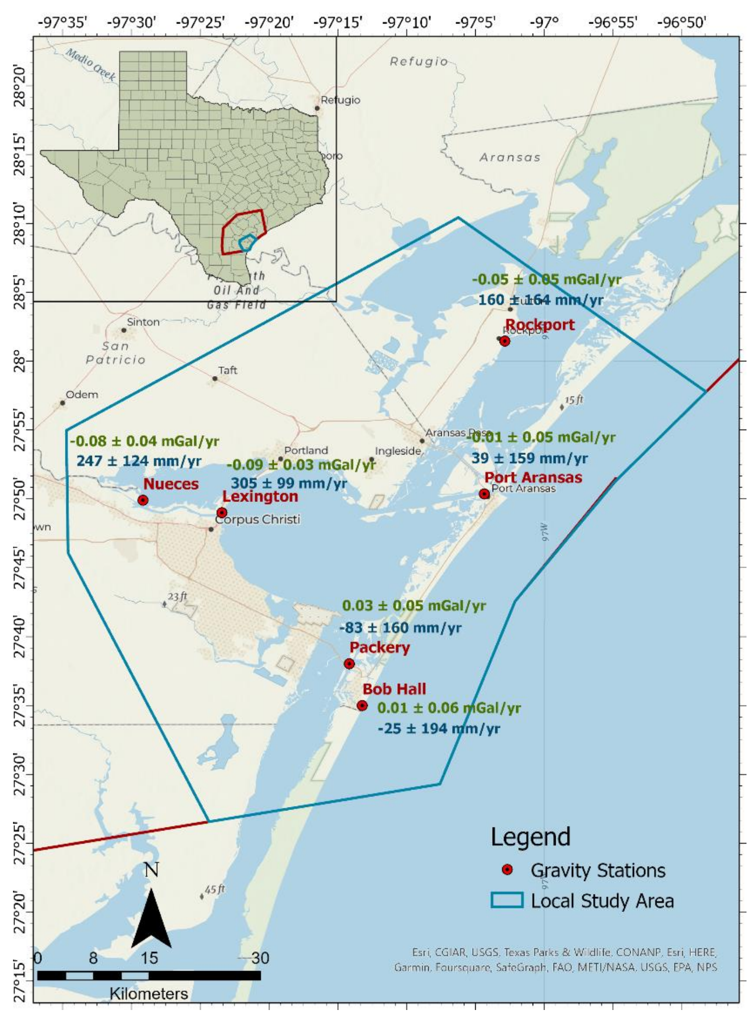

Figure 17: Map depicting spatial variability in gravity trends (mGal/yr; green) and gravity-derived height (mm/yr; blue).

According to gravity-derived rates, the station that subsided the most was Packery, at -83 ± 160 mm/yr. This was followed by Bob Hall Pier at -25 ± 194 mm/yr. Both stations displayed low significance, however, with values of 0.5 at Packery Channel and 0.8 at Bob Hall (Figure 18a-18b). These stations are both located on North Padre Island in the southern portion of the local study area (Figure 17).

The gravity-derived deformation rates revealed Lexington to be the station that witnessed the most dramatic trend in uplift, with a rate of 305 ± 99 mm/yr. The Nueces station followed, with a rate of 247 ± 124 mm/yr, then Rockport at 160 ± 164 mm/yr, and finally Port Aransas with a rate of 36 ± 159 mm/yr. Lexington and Nueces' rates were significant at 0.004 and 0.05 respectively, while Rockport (p-value 0.4) and Port Aransas (p-value 0.9) were not significant (Figures 18c-18f).

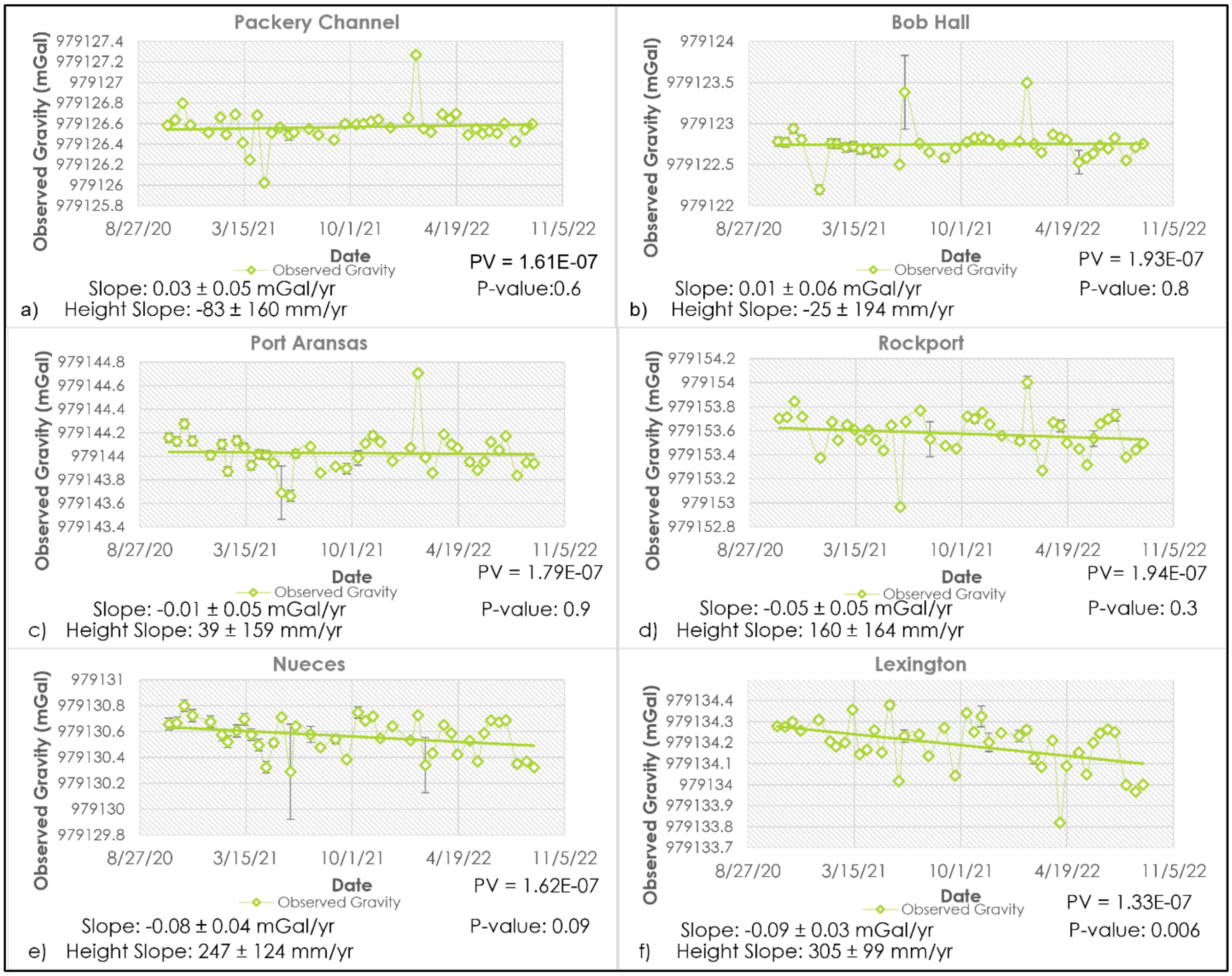

Figure 18: Temporal variability of gravity measurements and gravity-derived rates at gravity stations. Figures a-f show gravity trend in mGal/yr and disparity index at Packery Channel, Bob Hall Pier, Port Aransas, Rockport, Nueces, and Lexington respectively.

4.2.2 Land Subsidence Derived from Campaign GNSS Survey

The campaign GNSS survey took place from October 2020 to September 2022 at the six gravity stations in the local study area. The average campaign GNSS-based rate of deformation was -3 ± 13 mm/yr, and rates ranged from -18 ± 15 mm/yr at Bob Hall to 6 ± 9 mm/yr at Nueces. As displayed in Figure 19 stations located on the barrier islands (Packery at -1 ± 7 mm/yr, Bob Hall at -18 ± 15 mm/yr, Port Aransas at -10 ± 9 mm/yr) experienced subsidence according to the campaign GNSS derived rates, while the stations located further inland (Rockport at 0.3 ± 30 mm/yr, Nueces at 6 ± 9 mm/yr, Lexington at 3 ± 9 mm/yr) displayed uplift. The campaign GNSS results were not significant, with values ranging from 0.9 at Packery and Rockport to 0.2 at Bob Hall and Port Aransas (Figures 19). The temporal variability in the campaign GNSS-derived rates is shown in Figure 20. Examination of this figure indicates that the maximum variability is shown in Rockport, with a *PV* of 0.06, whereas the station with the least variability was Nueces, with a *PV* index of 0.009.

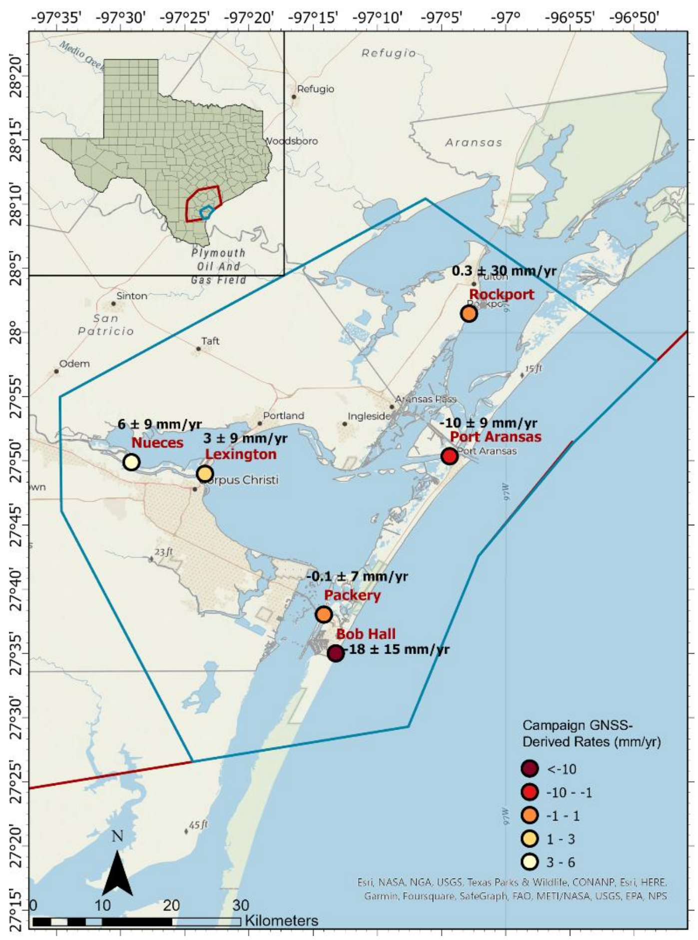

Figure 19: Map depicting spatial variability of campaign GNSS-derived deformation rates around the local study area in mm/yr. Dark colors indicate subsidence, light colors indicate uplift.

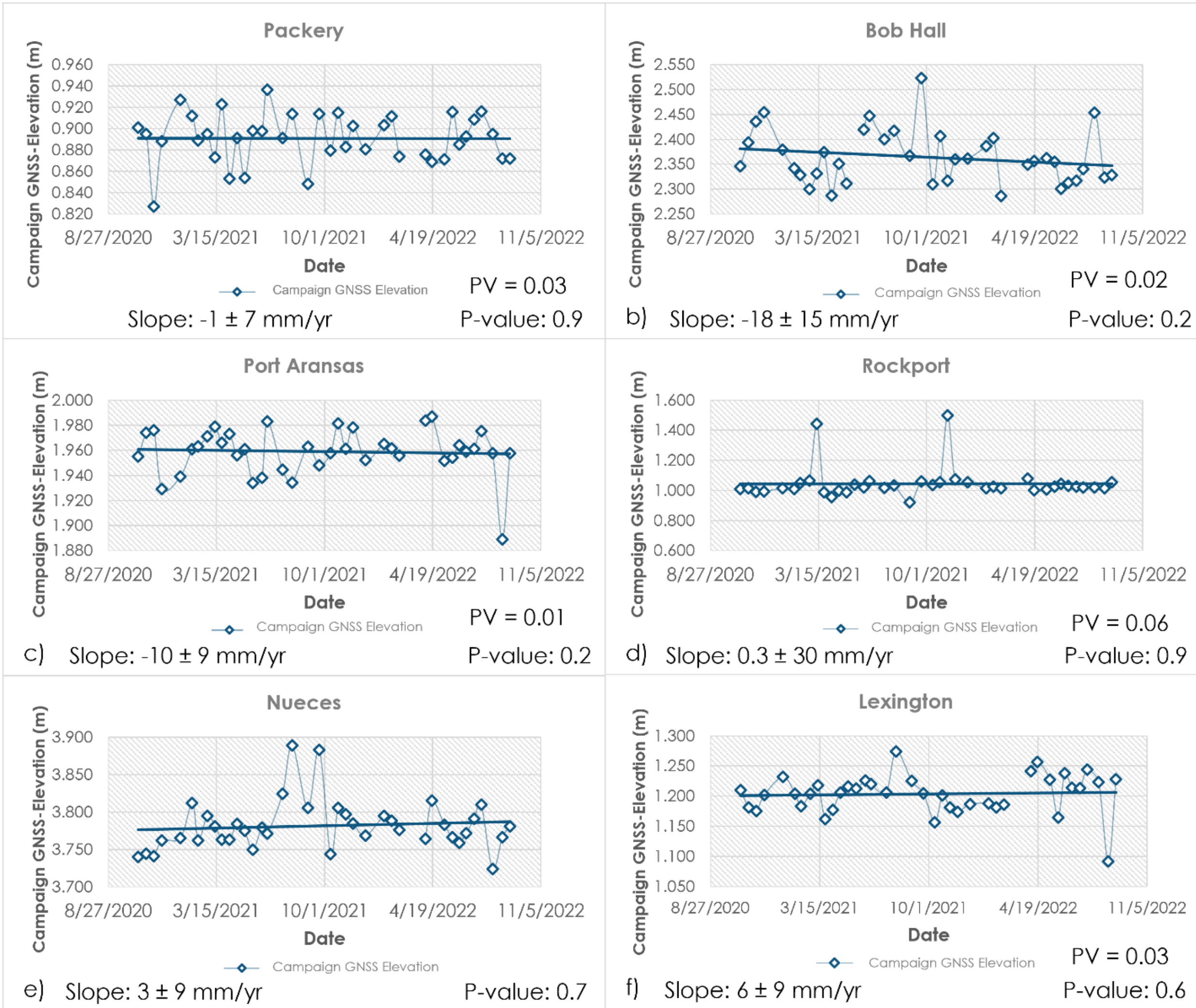

Figure 20: Temporal variability of campaign GNSS measurements. Figures a-f show campaign GNSS -derived trend in mm/yr and temporal variability at Packery Channel, Bob Hall Pier, Port Aransas, Rockport, Nueces, and Lexington respectively.

4.2.3 Results Derived from Permanent GNSS Stations

The permanent GNSS-derived vertical ground deformation rates extracted between January 2017 to September 2022 over the Coastal Bend are displayed in Figure 21. These rates were extracted from a total of fifteen permanent GNSS stations. The majority of the stations experienced subsidence over the study period. The average rate of displacement across the study area was -0.6 ± 0.1 mm/yr. Of the fifteen stations, ten displayed subsidence rates ranging from -0.09 ± 0.6 mm/yr to -15 ± 0.6 mm/yr. These stations were distributed both along the coast as well as further inland (Figure 21). Each station's rates were significant except for TXCU in Cuero

(Figure 22e), which displayed a p-value of 0.2. The station with the most dramatic subsidence trend was TXKC located in Karnes City, with a rate of -15 ± 0.6 mm/yr (Figure 23h).

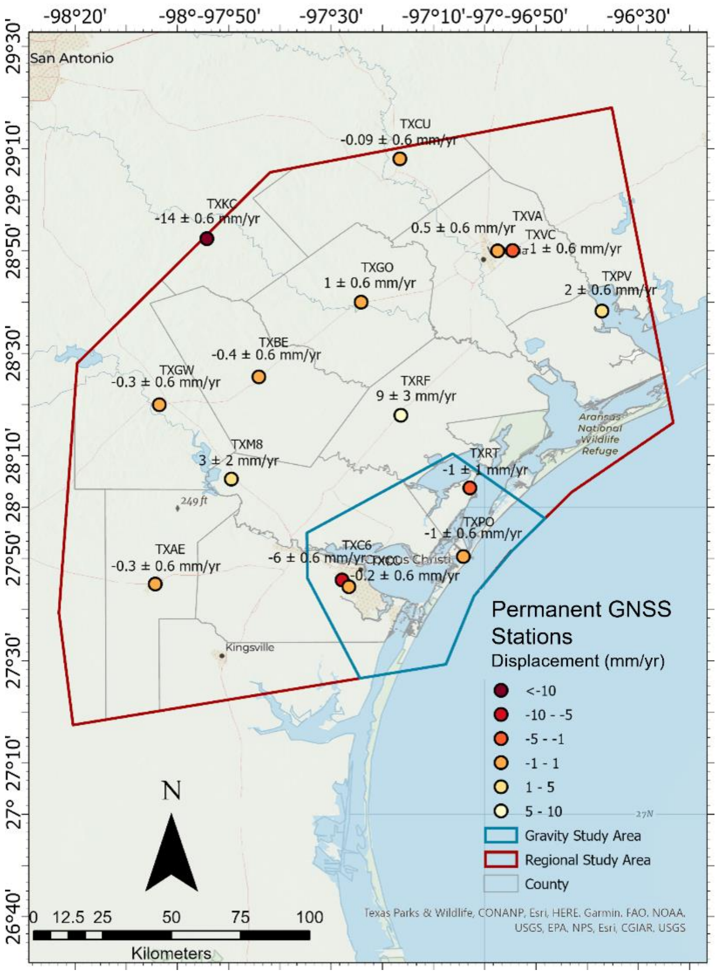

Figure 21: Map depicting spatial variability of permanent GNSS-derived deformation rates around the regional study area in mm/yr. Dark colors indicate subsidence, light colors indicate uplift.

Five permanent GNSS stations experienced positive deformation trends, indicating uplift. These rates ranged from 0.5 ± 0.6 mm/yr in Victoria (TXVC; Figure 22o) to 9 ± 2.8 mm/yr in Refugio (TXRF; Figure 22l). These stations (TXPV, TXVC, TXGO, TXRF) area located in bordering counties mainly on the eastern portion of the study region, and the only other station reporting uplift is at the western end of San Patricio County (Figure 21). Each station's rates were highly significant (Figure 22). The maximum variability is shown in TXC6, with a *PV* of 0.1 (Figure 22c), whereas TXCU (*PV* = 0.008) displayed no little to no variability (Figure 22e).

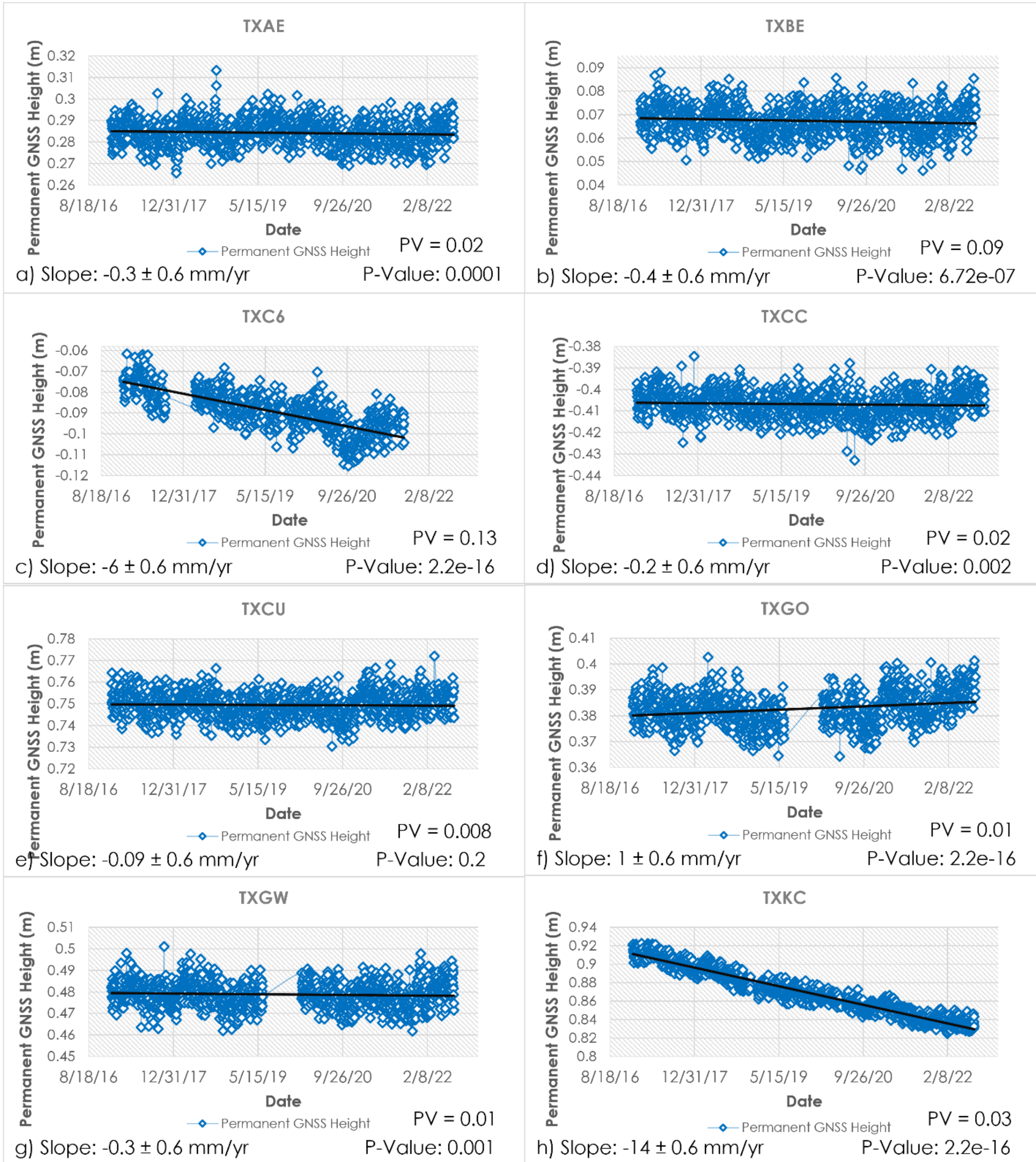

Figure 22: Temporal variability of permanent GNSS measurements. Figures a-o show permanent GNSS-derived trends in mm/yr and proportional variability PV.

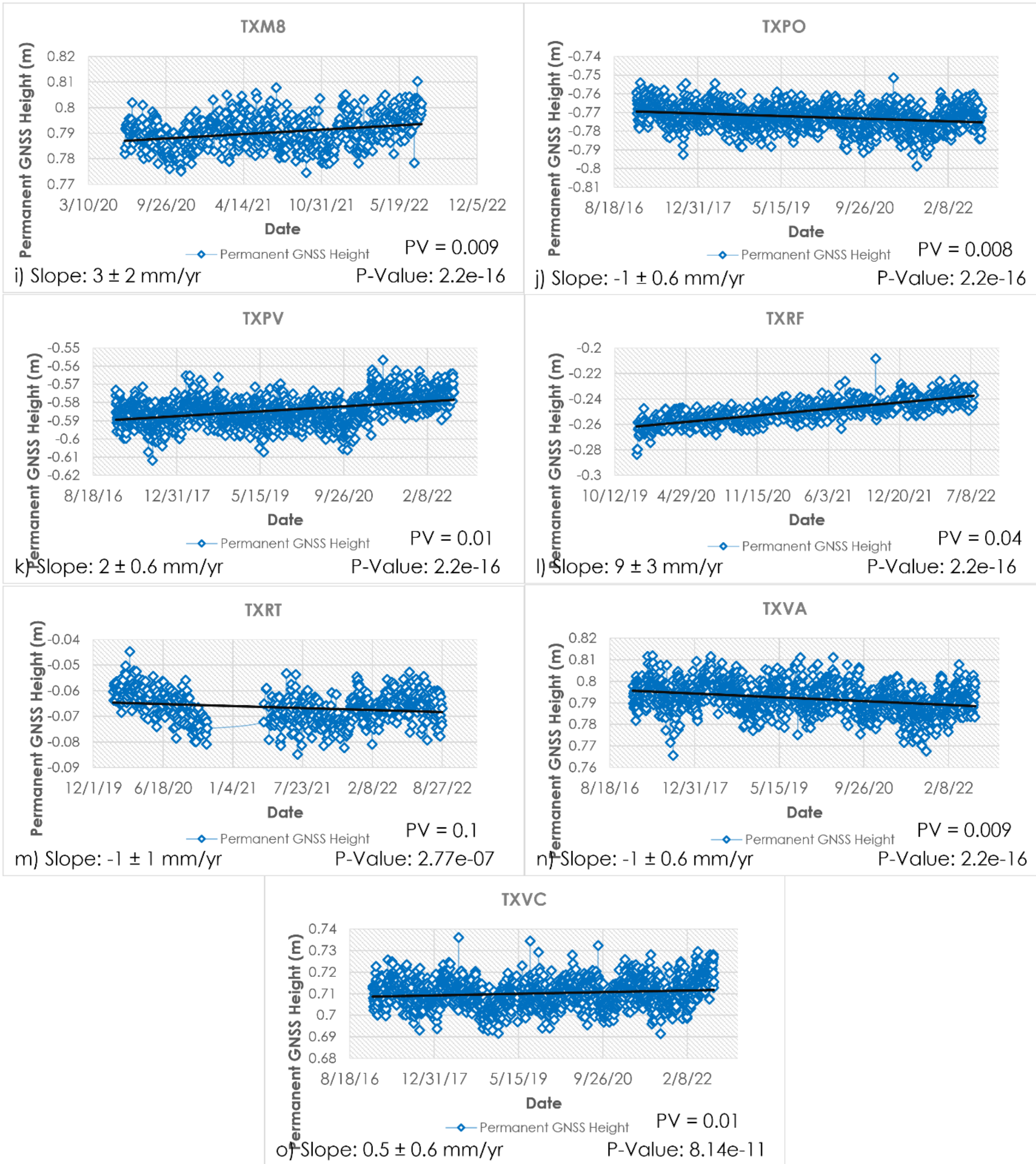

Figure 22: Continued.

4.2.4 Results Derived from InSAR

The Sentinel-1 InSAR-derived ground deformation rates extracted over the regional study area from January 2017 to November 2021 are displayed in Figure 23. Due to the nature and limitations of SAR imagery, coherence over agriculture/range/forest areas is lower, thus pixels displaying velocities were mainly clustered in urbanized areas. For this reason, the study area was classified into four categories: cities (CI), inland towns (IT), coastal towns (CT), and industrial plants (IP) (Figure 23). This classification was based on three main factors, including the population of the urban area for distinction between towns and cities (cities have populations over 50,000), the location to distinguish inland verses coastal areas, and type of urban use to distinguish the industrial plants such as refineries or steel/plastic/chemical plants. These areas were chosen based on visual observation of clustered InSAR pixels, and the polygons were created to include the majority of clustered InSAR pixels. Within each polygon, the average velocity of all the InSAR pixels located within that polygon was calculated, and standard deviation was calculated to represent the errors. Land deformation time series plots were also generated using ENVI's time series analyzer tool (Figures 24-27). The blue line represents the maximum value of displacement within a polygon, the black line represents the average value of displacement within a polygon, and the red line represents the minimum value of displacement within a polygon. Across all categories, the average displacement rate was 0.5 ± 3 mm/yr, with the highest rate of subsidence reaching -8 ± 6 mm/yr, and the highest rate of uplift being 10 ± 3 mm/yr.

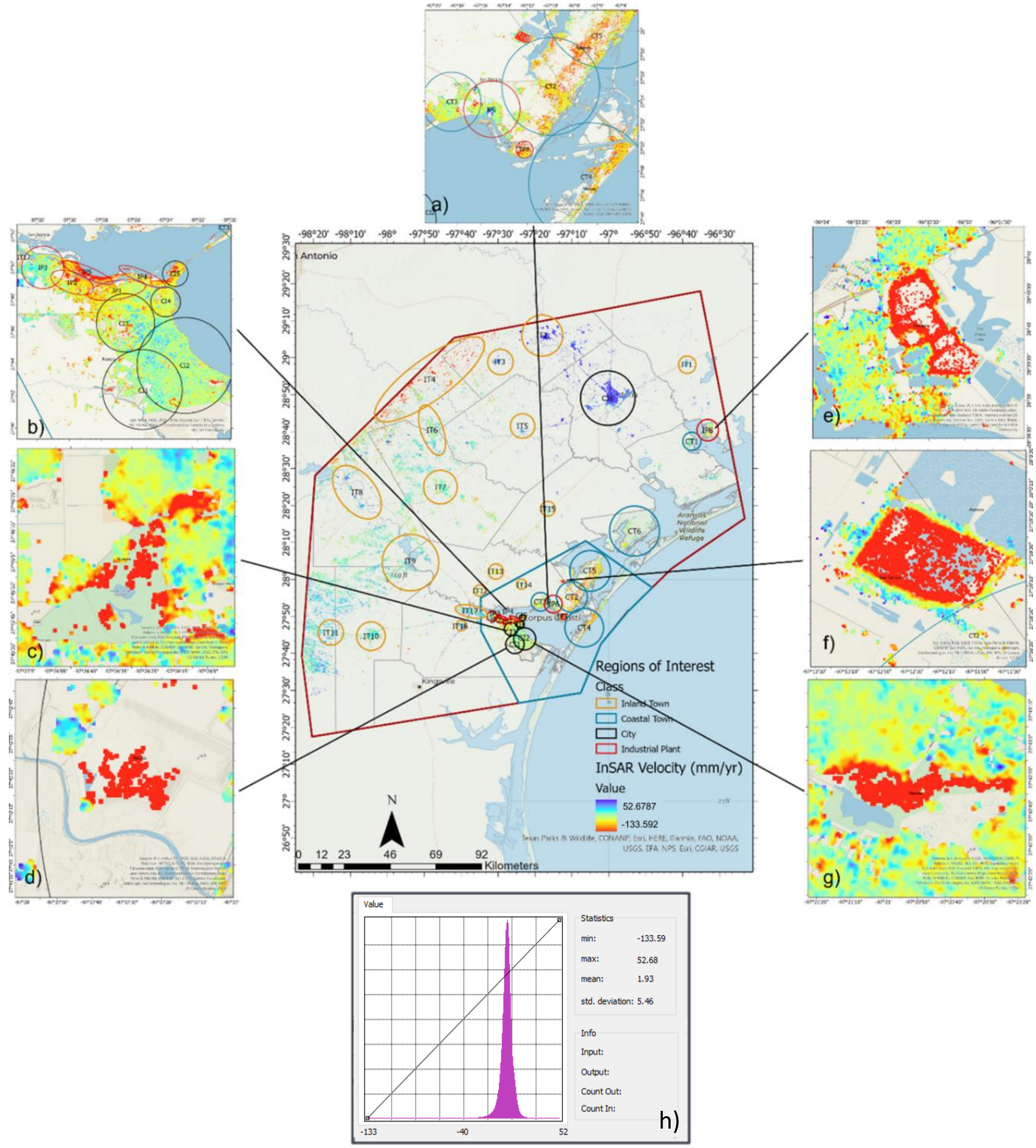

Figure 23: InSAR-derived land deformation rates (in mm/yr) generated over the Coastal Bend of Texas from January 2017 to November 2021. Yellow to red coloring indicates subsidence, while teal to blue indicates uplift. The four classes of areas are categorized as follows: Inland Town = IT; Coastal Town = CT; City = CI; Industrial Plant = IP. Insets: a) shows magnified regions of interest around the northern side of Corpus Christi Bay. b) shows magnified regions of interest in Corpus Christi and the Industrial Canal. c) displays Lozano golf course. Inset d) the JC Elliot landfill. e) shows the industrial plant at Point Comfort. f) shows Tailing Pond. g) shows the Nile golf course. h) shows the histogram of InSAR-derived land deformation rates.

Of the twenty-three towns encompassed within the regional study area, six bordered coastal water bodies and were classified as coastal towns. The coastal towns experienced an average displacement rate of -0.9 ± 3 mm/yr. Four of the six coastal towns (CT2, CT3, CT4, CT5; Figure

24b – 24e) displayed subsidence within the range of -0.4 ± 3 to -3 ± 3 mm/yr, and two coastal towns (CT1, CT6; Figure 24a and 24f) showed positive trends of 3 ± 4 mm/yr and 1 ± 4 mm/yr, respectively. The maximum variability is shown in CT6, with a *PV* of 4 (Figure 24f), whereas CT2 (*PV* = 0.1) displayed the lowest variability (Figure 24b).

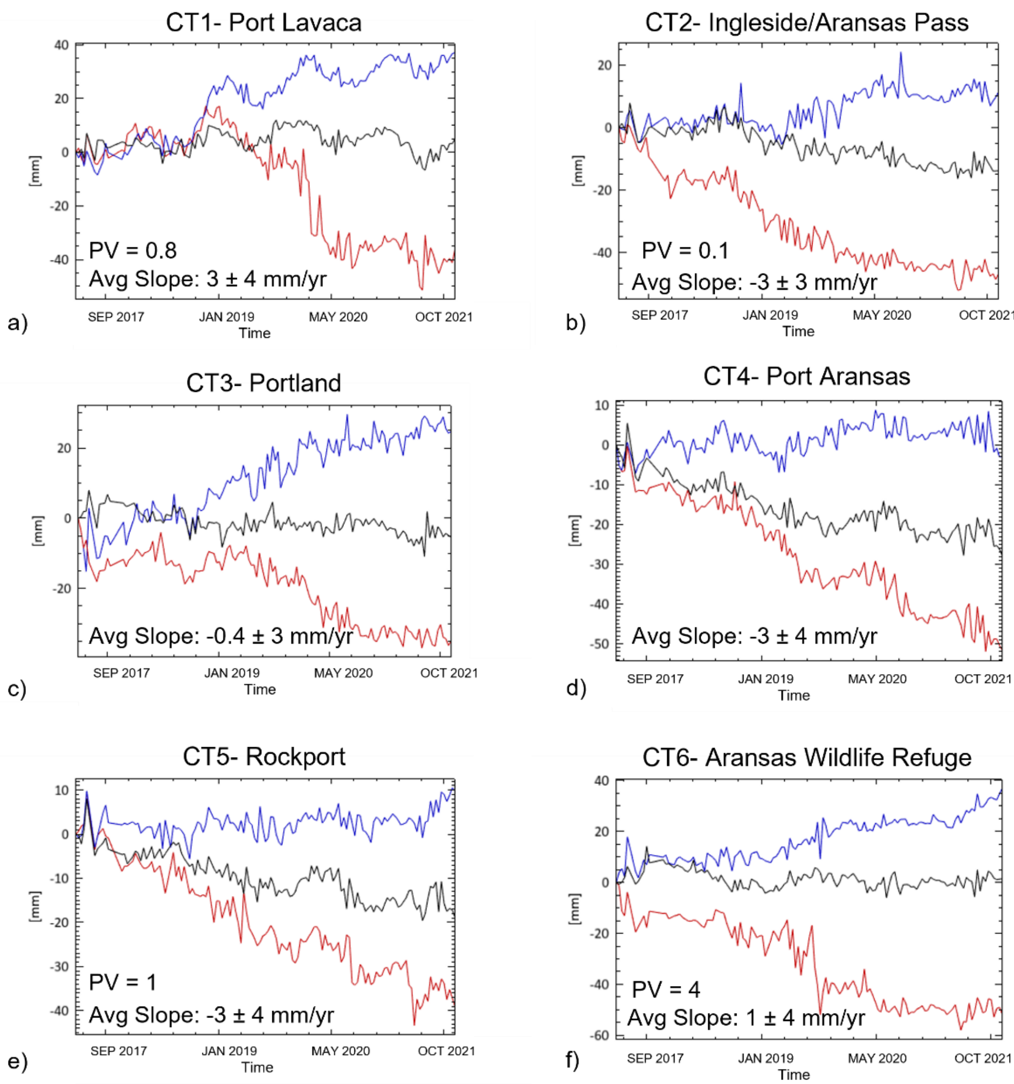

Figure 24: Time series plots generated for the areas classified as coastal towns. The time period is from January 2017 to November 2021. For each location, the black line represents the average displacement, blue represents the maximum value of displacement within the polygon, and red represents the minimum value of displacement within the polygon. The average slope was calculated by averaging all InSAR velocity points within the polygon, and error was determined by calculating the standard deviation. Graphs were generated using ENVI raster time series analyzer.

For the seventeen inland towns, the average rate of displacement was 2.6 ± 3 mm/yr. The majority of the inland towns displayed trends of uplift ranging from 2 ± 3 to 10 ± 4 mm/yr, while three inland towns (IT4 (Figure 25d), IT12, IT13 (Figure 25d and 25e)) showed subsidence rates ranging from -0.7 ± 3 to -8 ± 8 mm/yr. Examination of the figures below indicate that the maximum variability is shown in IT16, with a *PV* of 2 (Figure 25h), whereas the station with the least variability was IT12, with a *PV* index of 0.2 (Figure 25d).

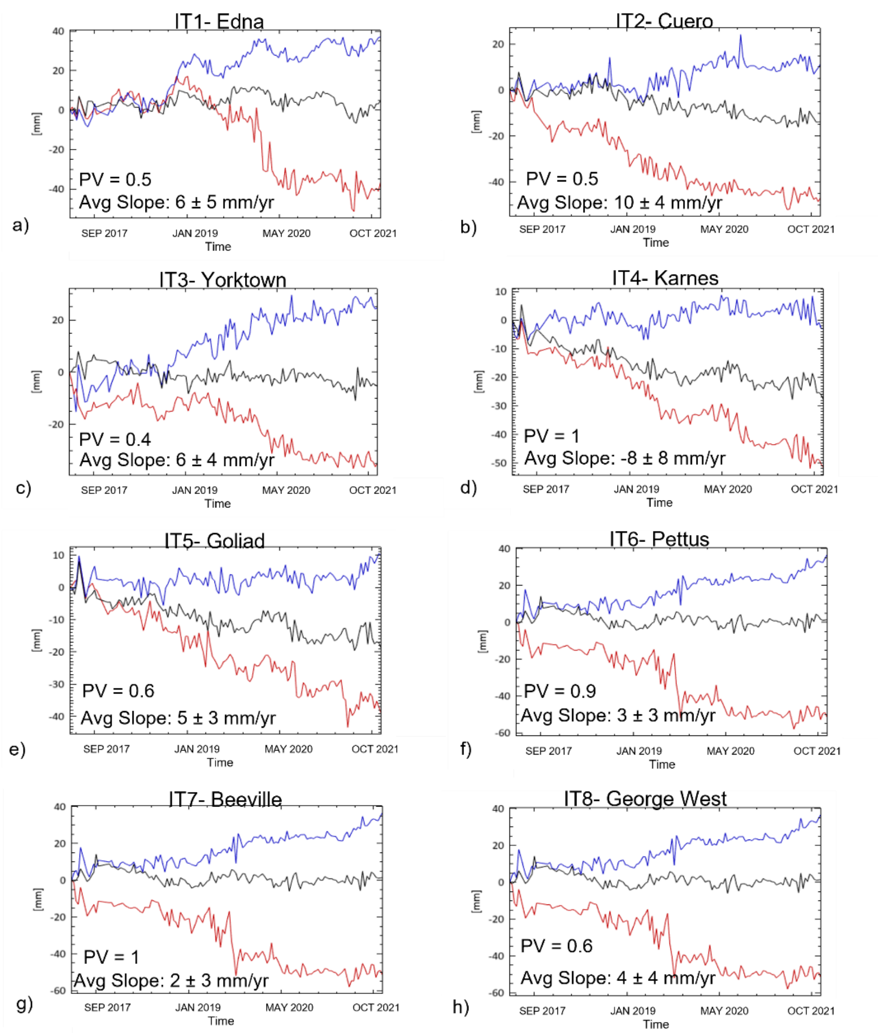

Figure 25: Time series plots generated for the areas classified as inland towns IT1-IT8. For each location, the black trend represents the average displacement, blue represents the maximum value of displacement within the polygon, and red represents the minimum value of displacement within the polygon. The average slope was calculated by averaging all InSAR velocity points within the polygon, and error was determined by calculating the standard deviation. Graphs were generated using ENVI raster time series analyzer.

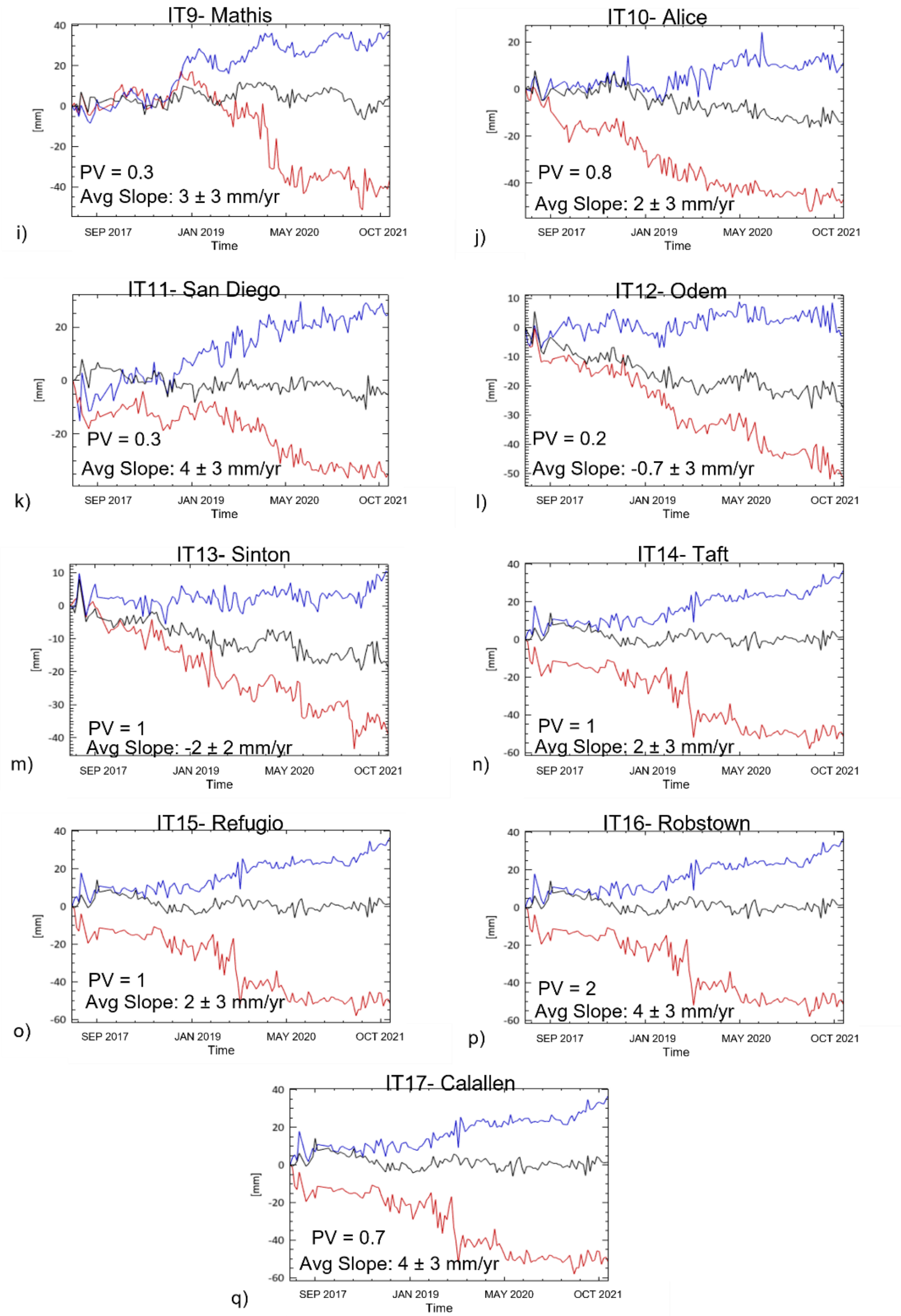

Figure 25: Continued.

Six regions were classified as city area, as they were part of Corpus Christi or Victoria. The cities experienced an average rate of displacement of -0.9 ± 3 mm/yr over the study period

(Figure 23). The areas that were part of Corpus Christi proper (CI3, CI4, CI5; Figure 26c-e) displayed negative trends of subsidence ranging from -0.2 ± 3 to -4 ± 3 mm/yr. The suburbs of Corpus Christi, CI1 and CI2 (Figure 26a-b), displayed positive displacement trends of 0.7 ± 2 mm/yr and 0.9 ± 2 mm/yr respectively. Victoria (CI6; Figure 26f), which is located further inland, reported a positive uplift rate of 8 ± 4 mm/yr. In the city bounds of Corpus Christi, three areas of interest were identified as undergoing increased rates of subsidence compared to the areas around them. These locations included two golf courses and a landfill (Figure 23). The golf courses were Nile Golf Course in Bay Area (CI2; Figure 23; inset g) and Lozano Golf Course in Central City (CI3; Figure 23; inset c), and these locations experienced rates of -12 ± 6 and -5 ± 5 mm/yr respectively. The JC Elliot Collection Center landfill (Figure 23; inset d) was located just outside of South Side (CI1), and reported an average of -35 ± 15 mm/yr with localized areas of subsidence up to -62 mm/yr.

Examination of the figures below reveal CI5 to be the location with the highest variability (*PV* = 11; Figure 26e), whereas the location displaying the lowest variability amongst the areas classified as city was CI2, with a *PV* index of 0.1 (Figure 26b).

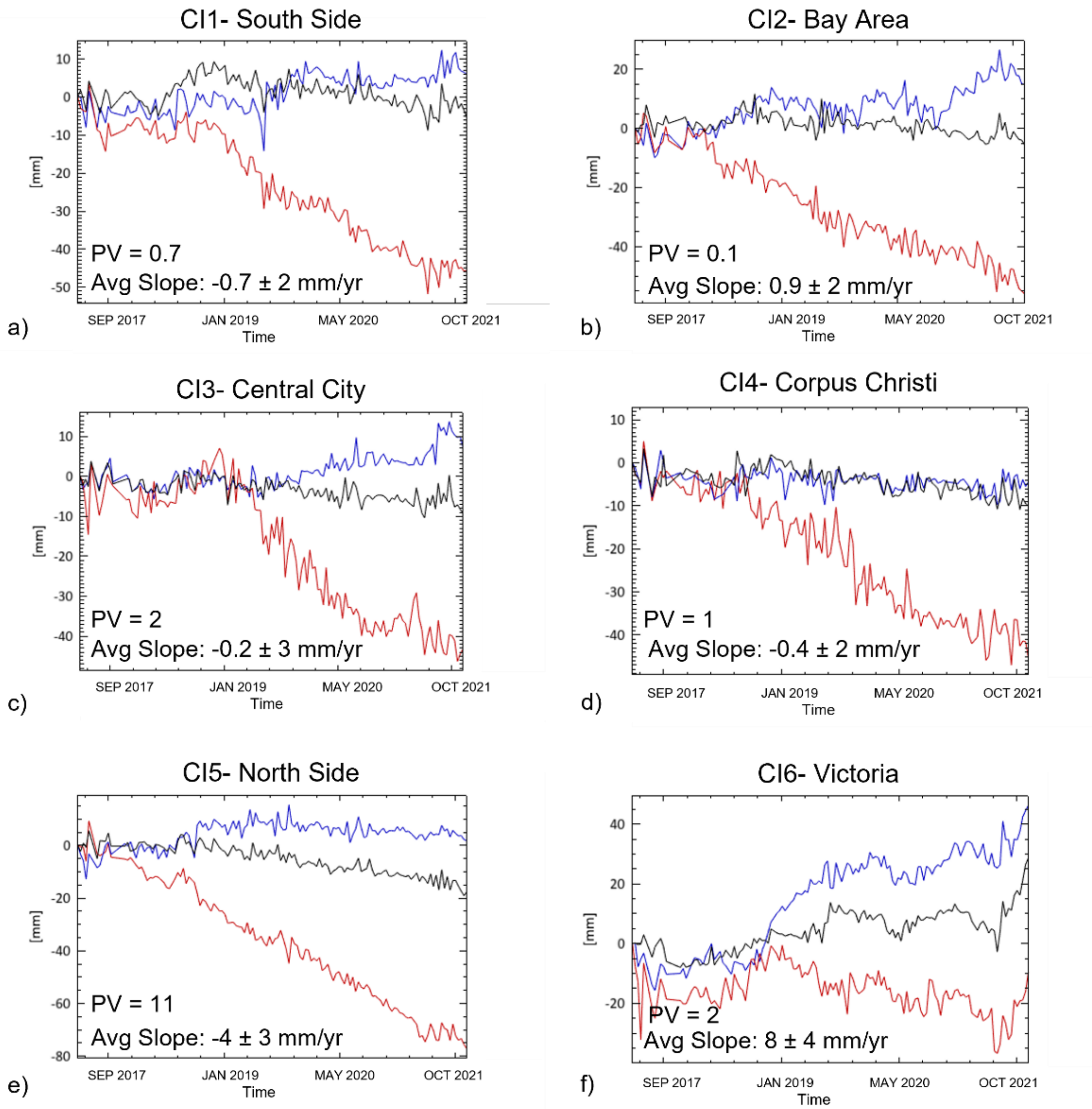

Figure 26: Time series plots generated for the areas classified as city CI1-CI6. For each location, the black trend represents the average displacement, blue represents the maximum value of displacement within the polygon, and red represents the minimum value of displacement within the polygon. The average slope was calculated by averaging all InSAR velocity points within the polygon, and error was determined by calculating the standard deviation. Graphs were generated using ENVI raster time series analyzer.

The industrial plants were differentiated from the rest of the urban areas due to their apparent increased subsidence rates. The average rate of displacement amongst this category was -3 ± 5 mm/yr. Out of eight identified industrial plants, seven displayed subsidence, ranging from -0.2 ± 5 to -8 ± 6 mm/yr. This was especially apparent in the plants along the Industrial Canal in

Corpus Christi (IP1-2 and IP4-5; Figure 27a-b Figure 27d-e), which had localized areas of subsidence reaching up to -42 mm/yr (Figure 23; inset a). Plant IP3 was the only plant to display a positive displacement trend, at 1 ± 2 mm/yr (Figure 27c). Plants IP6 and IP7 experienced rates of -0.2 ± 5 mm/yr and -5 ± 4 mm/yr, respectively (Figure 27f-g). The plant at Point Comfort (IP8; Figure 27h) had an average subsidence rate of -4 ± 16 mm/yr, the error likely coming from a small area within the extent of the plant which experienced extreme subsidence rates up to -133 mm/yr (Figure 23; inset e). Another area undergoing extreme subsidence was identified just outside of the IP6 and IP7. This location, Tailing Ponds Number 2, experienced subsidence averaging -14 ± 12 mm/yr, and with localized areas reaching up to -47 mm/yr (Figure 23; inset f). Amongst the industrial plants, the location displaying the highest variability was IP4, with a PV index of 2 (Figure 27d), while the plant with the lowest variability was IP2, with a PV index of 0.2 (Figure 27b).

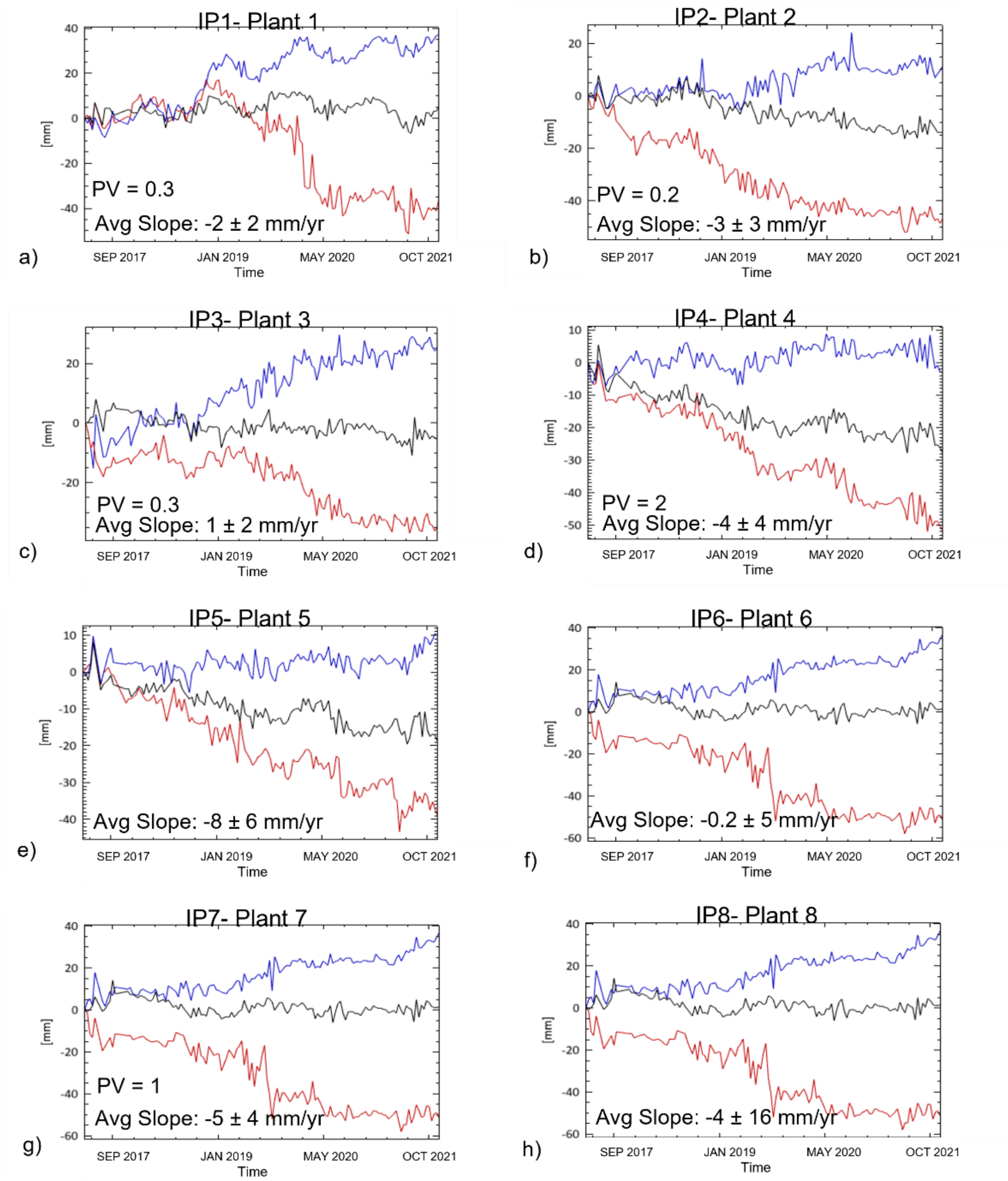

Figure 27: Time series plots generated for the areas classified as industrial plants. For each location, the black trend represents the average displacement, blue represents the maximum value of displacement within the polygon, and red represents the minimum value of displacement within the polygon. The average slope was calculated by averaging all InSAR velocity points within the polygon, and error was determined by calculating the standard deviation. Graphs were generated using ENVI raster time series analyzer.

4.3 Correlation and Validation Between Datasets

The individual datasets were correlated to each other based on the following criteria: regional or local scale; availability of data records; frequency of data collection; similar time periods of data acquisition; and proximity to nearest data points from other datasets. For this reason, the following section will be divided into results for the regional study and the local study. The regional study includes correlation between the InSAR and permanent GNSS results, and the local study includes correlation between gravity and campaign GNSS. InSAR and permanent GNSS were correlated because the InSAR velocities were able to be extracted over the same locations as the permanent GNSS stations, and the two datasets have the same acquisition time period. Gravity and campaign GNSS were compared because the measurements for the surveys were taken at the same time at the same locations.

4.3.2 Regional Study

The InSAR derived rates were compared to the rates derived from the fifteen permanent GNSS stations around the study area. Figure 28 depicts a scatter plot of the deformation rates extracted from InSAR and permanent GNSS plotted along a 1:1 line to show a decent correlation. InSAR points within a 150 m radius of the permanent GNSS station were averaged to extract these rates. A correlation coefficient of 0.7 was calculated between these two datasets, indicating a moderately positive relationship.

InSAR and permanent GNSS derived rates from TXCU and TXVA (Cuero and Victoria respectively) experienced the greatest differences from their respective paired stations. TXCU reported a difference of 12 mm/yr and TXCU reported a difference of 9 mm/yr. Other stations with notable differences of >5 mm/yr included TXC6 (5 mm/yr), TXGO (6 mm/yr), and TXVA (8 mm/yr).

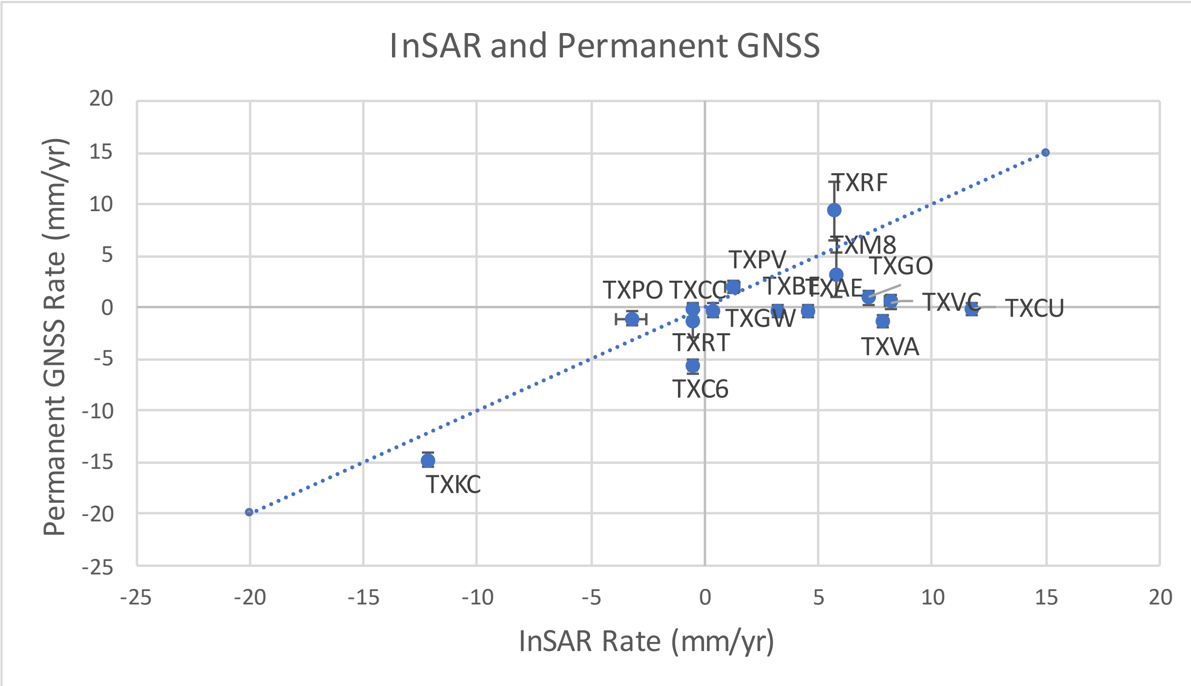

Figure 28: Correlation of InSAR derived and permanent GNSS derived land deformation rates (R: 0.7). Dashed line represents the 1:1 line.

4.3.4 Local Study

Gravity- and campaign GNSS-derived ground deformation rates were compared at each gravity station (Figure 29). A correlation coefficient of 0.7 was calculated between these two datasets, indicating a high positive relationship trend between results derived from these two techniques. In general, the campaign GNSS- and gravity-derived results reported subsidence rates in the same locations, namely Packery and Bob Hall. However, the campaign GNSS-derived results also showed that Port Aransas experienced subsidence of -10 ± 9 mm/yr, while the gravity-derived rate for that location was around 39 ± 159 mm/yr.

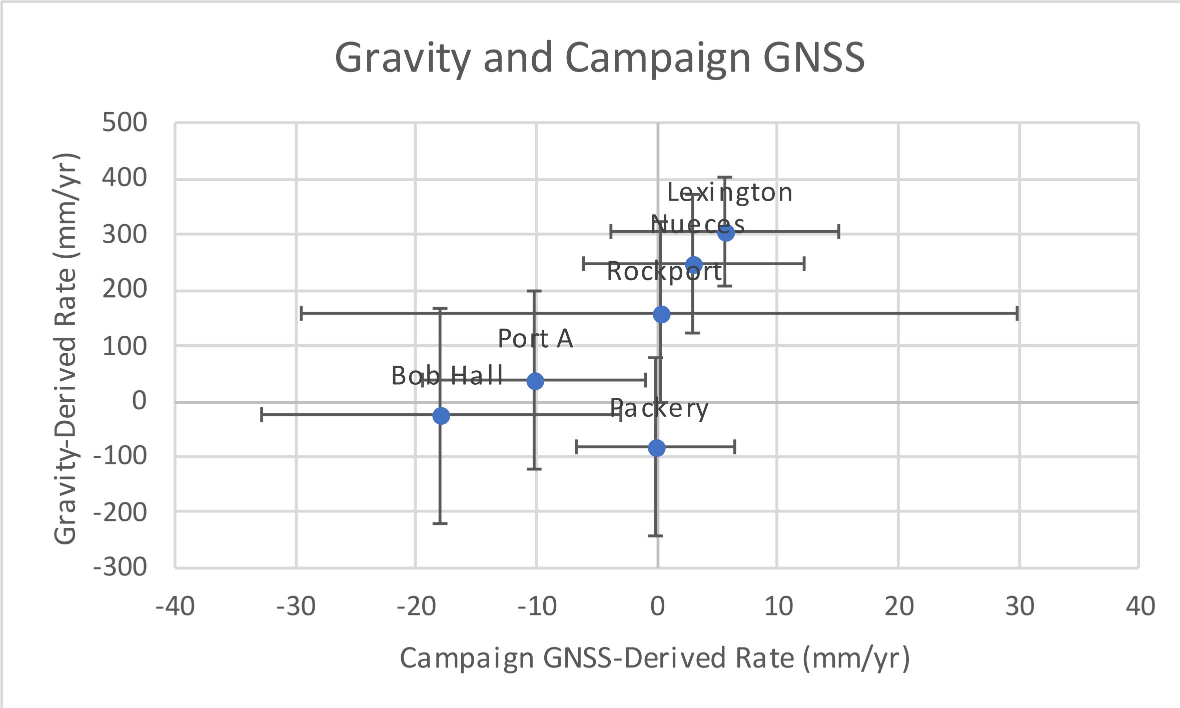

Figure 29: Correlation of gravity-derived and campaign GNSS-derived land deformation rates extracted over the local study area (R: 0.7).

4.4 Factors Controlling Land Subsidence

For this section, the controlling factors of observed subsidence rates were investigated. The velocity rates generated by InSAR (Figure 23h) were used to investigate the factors driving observed subsidence because these rates had good correlation with the permanent GNSS-derived rates (R = 0.7). Additionally, InSAR had a long study period and the most spatial coverage of the study area. This study only investigated areas undergoing subsidence. Areas experiencing uplift could be examined in a future study.

Four of the six coastal towns (CT2, CT3, CT4, CT5) experienced subsidence, with an overall average rate of -2 ± 3 mm/yr. These increased subsidence rates could be attributed to sediment compaction and growth faults. Areas CT2 and CT3 area located in San Patricio County, which experienced decreased extraction rates for both oil/gas (-5.3×10^7 BBL/yr; Figure 30a) and groundwater (-1.1×10^9 m^3/yr; Figure 30b) compared with their respective historic rates. The nearest groundwater monitoring well (Well 1; Figure 31a and 31b) reported a decrease in groundwater levels at a rate of -46 mm/yr. However, Well 1 is not directly in the proximity of these two locations, and the depth to water at this specific well may not be representative of the depth to the water table at CT2 and CT3. This area has moderate (0.05-0.1 km/km^2) growth fault density, so it is possible that observed subsidence in these areas could be due to growth fault intensity (Figure 30c). Area CT4 is part of Nueces County, which underwent a decrease in oil/gas extraction rates compared to the historic rates from this county (1.2 x 10^8 BBL/yr; Figure 30a). The groundwater extraction rates for this county increased compared to historic rates (3.5 x 10^8 m^3/yr; Figure 30b), and when compared to the closest groundwater monitoring well (Well 1; Figure 31a and 31b), the water level in this well decreased at a rate of -46 mm/yr. However, this location is situated on a barrier island and the groundwater extraction rates of the county as well as the depth to water from the nearest monitoring well are likely not representative of this isolated area. CT4 is in an area classified by moderate to low density growth faults (0-0.1 km/km^2; Figure 30c). Area CT5 is located in Aransas County, which underwent a decrease in groundwater extraction rates (difference of around -0.1 x 10^6 m^3/yr) during the study period compared to the historic groundwater extraction rates (Figure 30b). The groundwater monitoring well was located within this area decreased at a rate of -46 mm/yr (Well 1, Figure 31a and 31b). Oil and gas extraction rates decreased in this county compared to the historic rates (-2.3 x 10^7 BBL/yr; Figure 30a), so it is likely not a factor. This area is also located with a zone of moderate to low density growth faults (0-0.1 km/km^2; Figure 30c). However, all of the subsiding coastal towns are located on areas underlain by sand, silt, and clay (Figure 30d), so sediment compaction is likely the driving factor for subsidence within these areas.

The inland towns IT4, IT12, and IT13 experienced an average subsidence rate of -4 ± 4 mm/yr. For IT4 (located in Karnes County), increased groundwater extraction is most likely the driving factor behind the subsidence, as Karnes County experienced the highest increase in groundwater extraction rates of all the counties in the study area, with an increased rate of 2.7 x 10^9 m^3/yr (Figure 30b). A groundwater monitoring well in the area showed an increase in water level at a rate of 964 mm/yr (Well 3; Figure 31a and 31b). This county experienced a decrease in oil/gas extraction rates compared to historic rates (<-29 x 10^7 BBL/yr; Figure 30a). It is located in an area characterized by a low density of growth faults (0-0.05 km/km^2; Figure 30c) and underlain primarily by sandstone (Figure 30d). For IT12 and IT13, the driving factor behind the observed subsidence is likely due to sediment compaction, as the area is underlain by clay, silt, and sand (Figure 30d), as well as the high density of growth faults (0.1-0.2 km/km^2; Figure 30c). Fluid extraction is likely not the driving factor in these two towns, as both oil/gas and groundwater extraction rates decreased in San Patricio County compared to the respective historic extraction rates (-5.3 x 10^7 BBL/yr;Figure 30a, -1.1 x 10^9 m^3/yr; Figure 30b). The nearest groundwater monitoring well showed a decrease in water level over the study period, with a trend of -41 mm/yr (Well 6; Figure 31a and 31b,). A secondary well was found near that location, and it showed a slight increase in water level with a slope of 16 mm/yr (Well 4; Figure 31a and 31b).

Of the six areas classified as city, three displayed land subsidence, including CI3, CI4, CI5. These areas were all located around Corpus Christi Proper, which displayed an average subsidence rate of -1 ± 2 mm/yr. The driving factors of the observed subsidence in this area could be attributed to sediment compaction due to moderate intensity of growth faults, and possibly accelerated groundwater extraction rates. It is not likely due to oil/gas extraction, as the extraction rates during the study period decreased compared to the historic rates from this county (1.2 x 10^8 BBL/yr;

Figure 30a). Nueces County is located in a region primarily consisting of sand, silt, gravel, and clay (Figure 30d) and overlapped by a moderate density of growth faults (0.05-0.1 km/km^2; Figure 30c). Additionally, the county experienced a high increase in groundwater extraction rates compared to the historical period (3.5×10^8 m^3/yr; Figure 30b).Two groundwater monitoring wells were found in the vicinity of these areas (Wells 5 and 6; Figure 31a and 31b), and one showed an increased water level over the study period at a rate of 50 mm/yr (Well 5), while the second showed a decrease in water level over the study period at -35 mm/yr (Well 6). Within CI1, CI2, and CI3, there were three areas of interest in which heightened subsidence rates were recorded. These include two golf courses at Lozano and Nile (Figure 23; inset c and g), in which rates were -5 ± 6 and -12 ± 6 mm/yr respectively. The other location was at the J.C. Elliot landfill (Figure 23; inset d). Google Earth images were retrieved over these three areas from 2017 to 2022 (Figure 32a-c), and visual inspection of the images compared with InSAR-derived velocity rates over time reveals that there has been no visible land surface change over time, whether through construction of change in land use. Because of this, it is thought that the driving factor of subsidence in these three locations is sediment compaction.

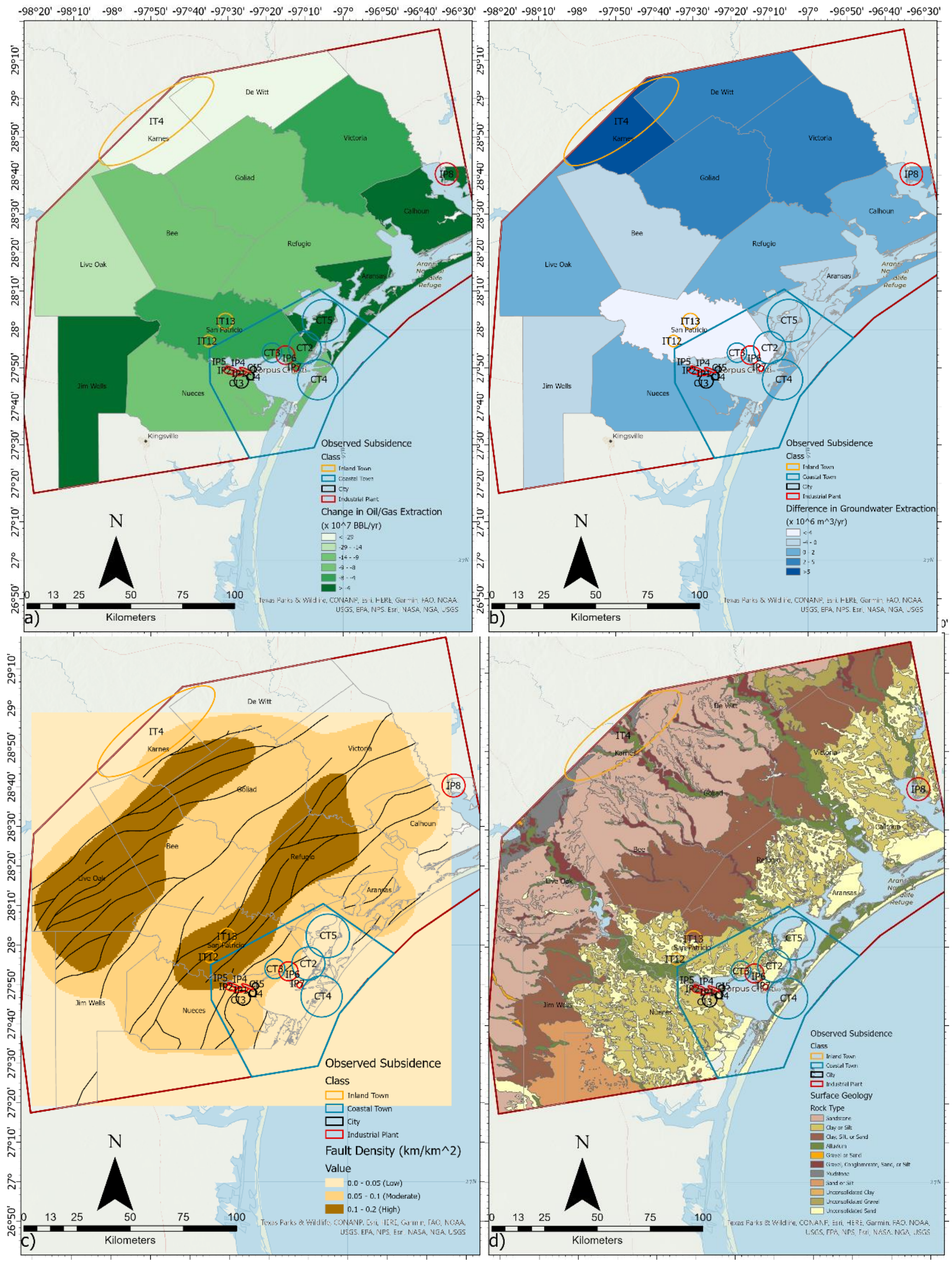

Figure 30: Spatial distribution of observed areas of subsidence, generated from InSAR, correlated with a) difference in oil and gas extraction rates averaged by county between the study period and historical period (BBL/yr), b) difference in groundwater extraction rates averaged by county between the study period and historical period (m^3/yr), c) growth fault density (km/km^2), and d) surface geology.

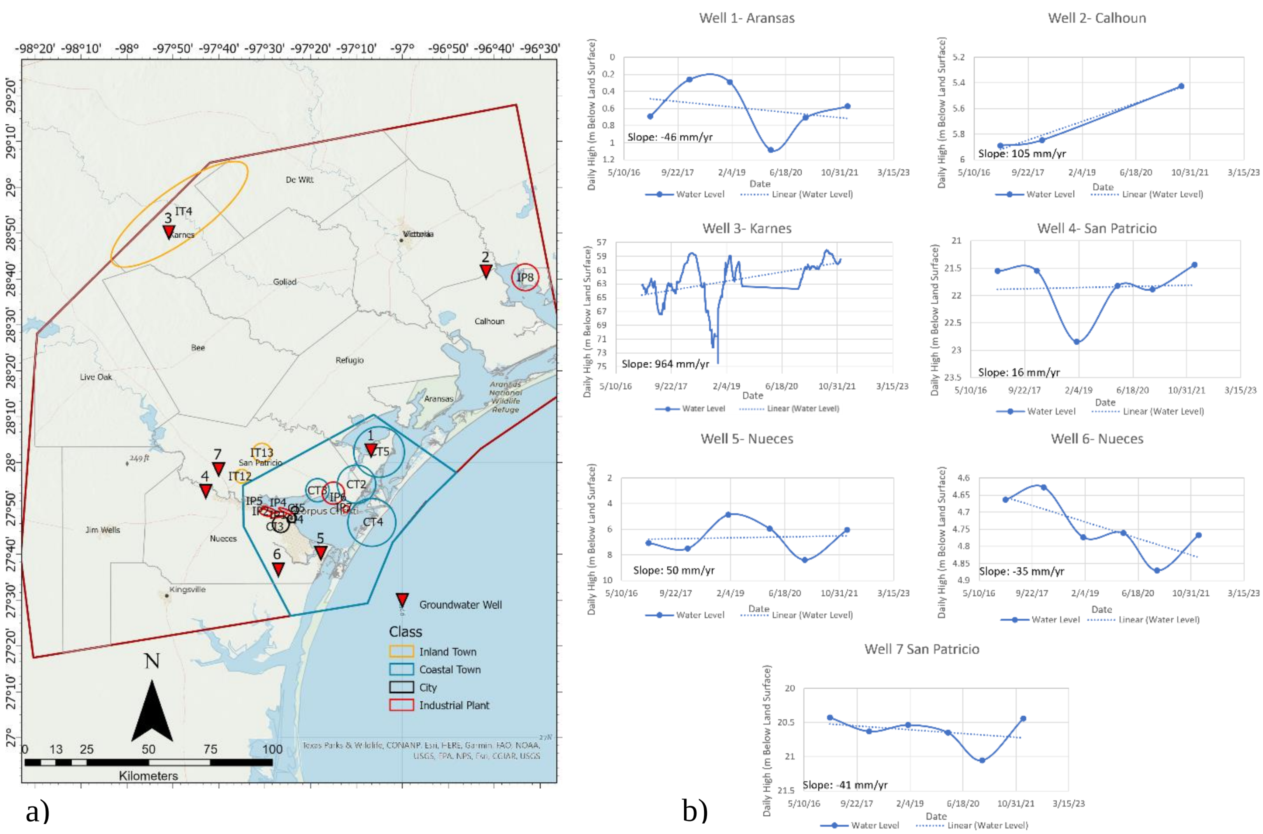

Figure 31: a) Locations of groundwater monitoring wells around some of the subsiding areas. These wells were chosen based on location and availability of data. b) Timeseries of the annual groundwater levels from January 2017 to January 2022.

Seven of the eight areas identified as industrial plants experienced subsidence, with an average rate of -4 ± 6 mm/yr. Plants IP1-2 and IP4-5 are located along the industrial canal in Corpus Christi, an area in Nueces County discussed previously as experiencing increased rates of groundwater extraction, sitting atop unconsolidated sediments, and consisting of moderate (0.05-0.1 km/km^2) growth fault density. However, the plants at IP6, IP7, and IP8 area in different regions and are in low density growth fault areas (0-0.05 km/km^2; Figure 30c). Plants IP6 and IP7 are located in San Patricio County, which saw decreased fluid extraction rates compared to the historic periods (-5.3 x 10^7 BBL/yr (Figure 30a); -1.1 x 10^9 m^3/yr (Figure 30b)) and has a moderate to low density of growth faults (0-0.1 km/km^2; Figure 30c). The area is characterized by unconsolidated sand as well as clay and silt. The plant at IP8 is located in Calhoun County, which is experiencing an increased rate of groundwater extraction compared to the historical period (5 x 10^7 m^3/yr; Figure 30b). However, this rate may not be representative of IP8 itself, so though groundwater extraction rate is increasing, it may not be a driving factor of subsidence. A groundwater monitoring well was located near the city of the plant, and the well reported an increase in water levels over the study period, with a rate of 105 mm/yr (Figure 31a and 31b, Well 2). IP8 is located in an area that has a low density of growth faults (0-0.05 km/km^2; Figure 30c), but it is underlain by clay and silt (Figure 30d). It is thought that the main driving factor of subsidence at these plants could be sediment compaction by overburden from steel stacks and storage tanks. This could also be a contributing factor to subsidence at the plants located along the industrial canal in Nueces County (IP1-2 and IP4-5). Google Earth images were retrieved over two plants along the Industrial Canal in order to show areas of increased subsidence in areas where there has been new construction of refinery stacks or storage tanks at IP2 (Figure 32d) and IP5 (Figure 32e). There were two additional areas of interest in which InSAR detected heightened rates of deformation. These locations were at Tailing Pond 2 near IP6 (Figure 23; inset f) and Point Comfort IP8 (Figure 23; inset e). Tailing Pond 2 recorded localized subsidence up to -47 mm/yr, while Point Comfort saw rates averaging -29 mm/yr (Figure 27h; red line). Google Earth images retrieved over these two areas from 2017 to 2022 reveal that there is no obvious change in land use or new construction (Figure 32f-g). Instead of natural subsidence, it is thought that the exposed sediments here area being scoured after they are initially laid as mud and then dry.

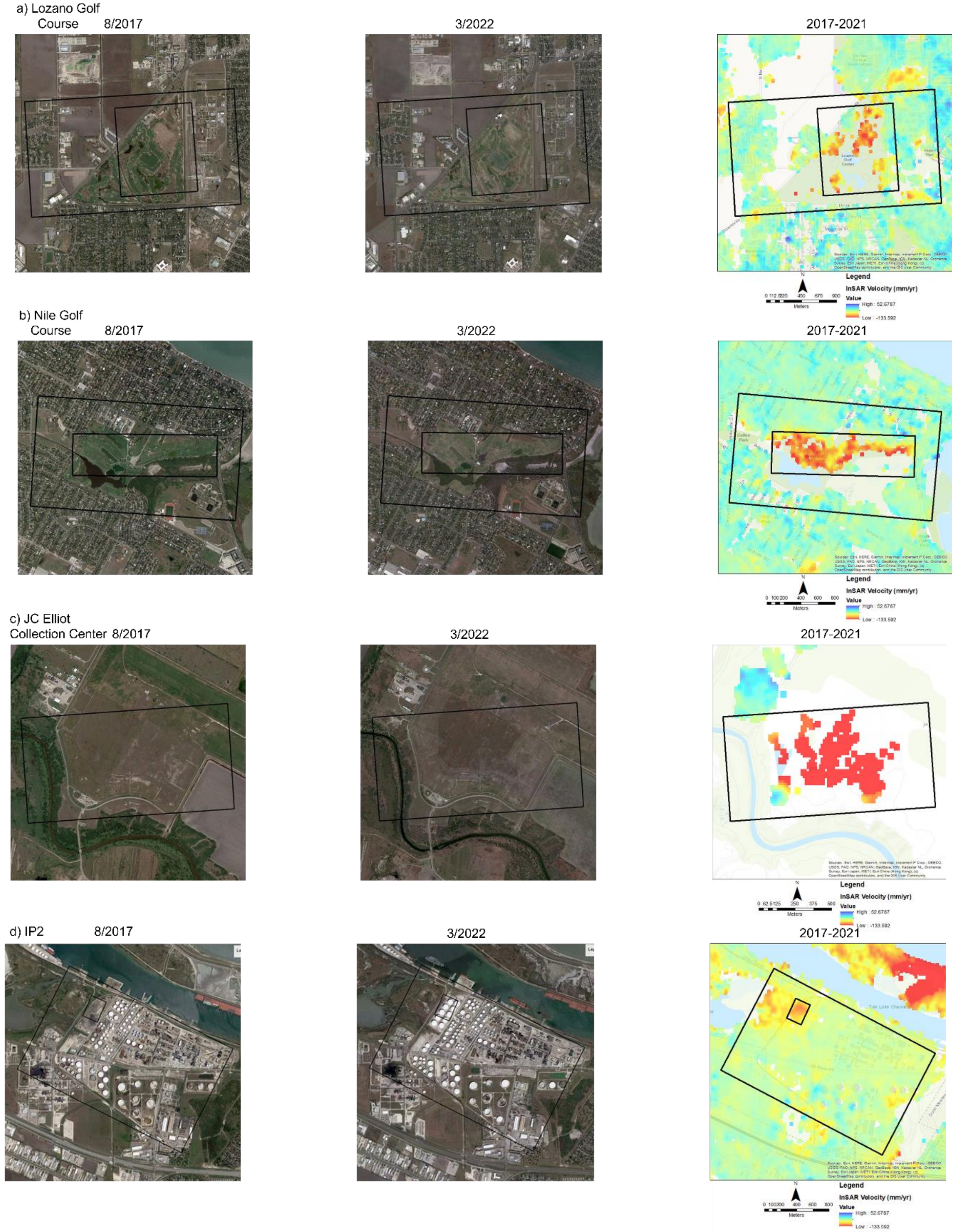

Figure 32: Historical Google Earth images and InSAR-derived land subsidence differences over a) Lozano Golf Course, b) Nile Golf Course, c) J.C. Elliot Collection Center, d) plant IP2, e) plant IP5, f) Tailing Pond 2, and g) the Point Comfort plant at IP8. The black rectangle within the polygon shows reference area of increased subsidence over time.

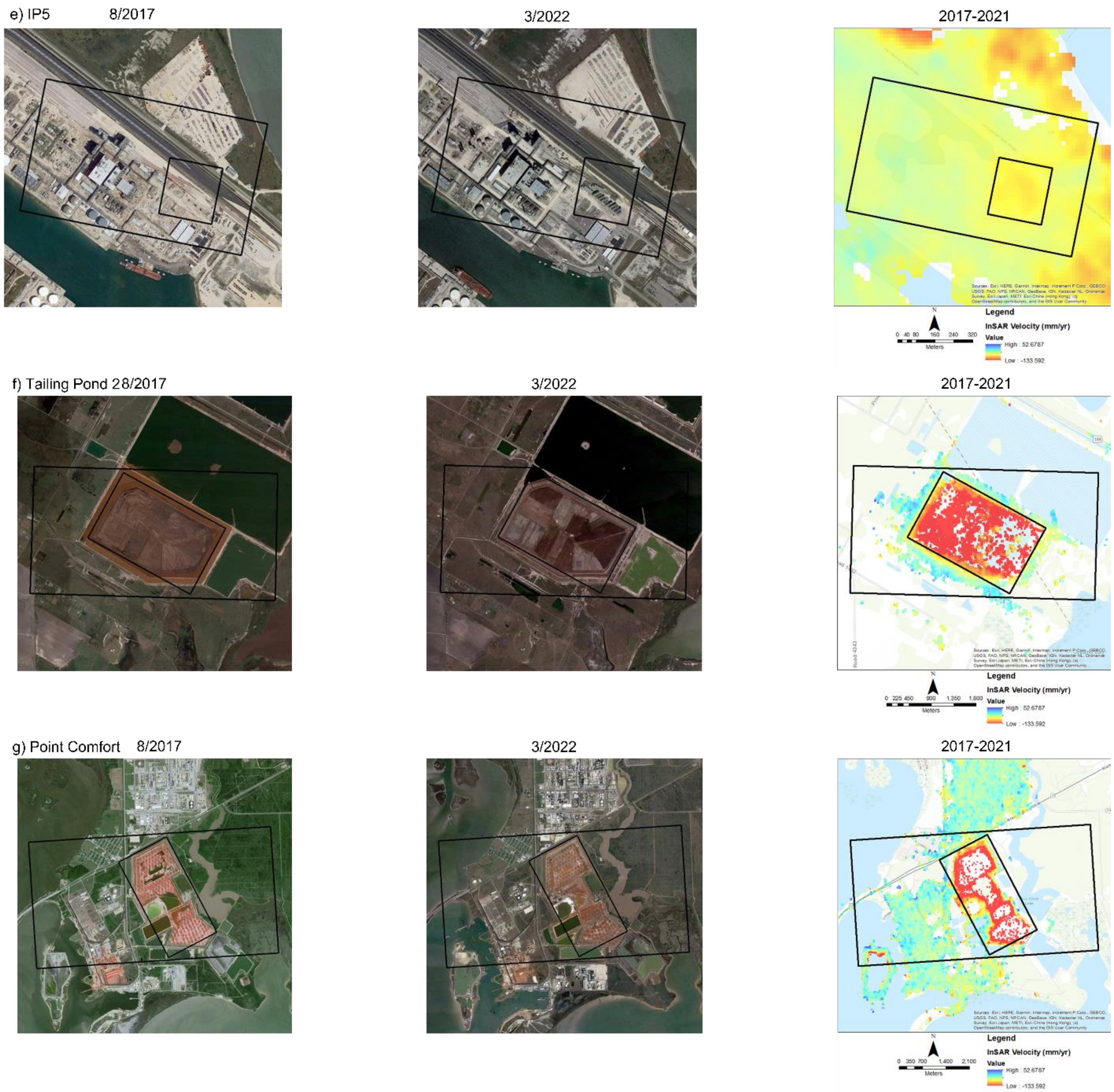

Figure 32: Continued.

CHAPTER V

DISCUSSION AND CONCLUSION

5.1 Discussion

This research integrated four independent techniques and datasets to generate new land subsidence datasets for the Coastal Bend of Texas on both local and regional scales. Results revealed that the observed regional subsidence patterns are likely driven by groundwater extraction and growth faulting. This is consistent with findings from previous studies that have been conducted around the Coastal Bend of Texas, in which subsidence has been found to be driven by increased groundwater extraction rates, sediment compaction, and growth faulting (Qu et al. 2015; Zhou et al. 2021; Haley et al. 2022).

The SBAS-InSAR technique is typically restricted to application in well-developed or non-vegetated areas. However, the InSAR-derived results in this study showed fair spatial coherence despite the rural nature of the study region. Additionally, there was moderately high correlation between the InSAR-derived and permanent GNSS-derived land deformation rates. This study verified that the SBAS technique has potential for quantifying deformation rates in other rural areas.

There were some limitations to this study. For the gravimetry technique, a limitation was the overall campaign period, as well as the frequency of the surveys. That is, the study period for the gravity campaign was from October 2020 to September 2022, and surveys were conducted every two weeks. Land subsidence is a long-term phenomenon, so a longer study period and more frequent surveys would help refine the rates to be more representative of local land deformation, as well as improve the significance of the trends. The error in the trends could be attributed to noise at the stations. The gravimeter is highly sensitive to movement, so noise could be attributed to nearby roads and highways, foot traffic from pedestrians, waves from nearby bodies of water, and weather effects like wind. Noise could be addressed by conducting the survey at quieter times of the day, such as early morning or later in the evening to avoid both automotive and pedestrian traffic. Conducting the surveys on days where there is calm weather, little wind, and still bodies of water would improve the results. While the employed gravimeter, with a reported accuracy of ±0.01 mGal, was sufficient for the purpose of this experiment, a more accurate instrument, such as the Scrintrex CG-6 gravimeter could be used. In addition, the technique could be improved with the employment of an absolute gravimeter instead of a relative gravimeter. Another limitation includes the base station, over which InSAR results revealed to have a subsidence rate of approximately -1 ± 0.8 mm/yr. Establishing a reference base station in a more stable location could improve the gravimetry results.

Similar to the gravity campaign, a limitation to the campaign GNSS survey was the short study period. Data should continue to be collected over time in order to accurately represent the deformation in the area. Additionally, some of the stations were located near buildings, trees, telephone poles, boats, and other structures that could interfere with the campaign GNSS signal. Taking campaign GNSS readings in a wide, open space with no structures around would improve the measurements.

Though the InSAR- and permanent GNSS-derived rates were consistent with each other, there are still a few limitations with the technique. For one, the study period over the regional study area (though longer than the gravity and campaign GNSS study period) could be longer. As mentioned before, land subsidence is a long-term phenomenon, and while the rates generated in this study are accurate, they may not be representative of the long-term pattens of subsidence. The time range of the InSAR study period could be extended by combining the Sentinel-1 data with datasets from other satellite platforms, such as Phased Array Type L-Band Synthetic Aperture Radar (PALSAR) or Environmental Satellite (ENVISAT).

Integration of the different methods and techniques was successful, specifically with the correlation of InSAR and permanent GNSS. Though the correlation was moderately high (R was estimated to be 0.7 between the two datasets), there are a few limitations when comparing these datasets. There are possible errors associated with InSAR processing such as orbital errors, low coherence, and unwrapping errors that could contribute to the inconsistency in correlation. Another factor could be the frequency at which data acquisition occurs. For example, permanent GNSS rates are calculated daily, while there are roughly three weeks between InSAR acquisitions. Despite these limitations, there was still good correlation between InSAR and permanent GNSS.

InSAR and permanent GNSS, however, could not be correlated with gravity and campaign GNSS. The biggest reason for this was the difference in the range of the study periods. The short length of the gravity and campaign GNSS study periods made it difficult to correlate results with the techniques that had longer study periods. Another reason they weren't correlated was the disparity in frequency of data collection amongst all datasets. Permanent GNSS takes continuous readings, Sentinel-1 provides imaging roughly every 3 weeks, the gravity and campaign GNSS surveys were conducted every two weeks. The last reason for not correlating all datasets with one another was the limited coverage of the gravity and campaign GNSS surveys, the limited availability of InSAR data in portions of the local study area, and the sparse distribution of permanent GNSS stations. Gravity and campaign GNSS results were only generated over six points around the Corpus Christi Bay, while the other two datasets covered areas up to 150 km inland. InSAR data was unavailable for the area over North Padre Island, specifically the Packery and Bob Hall gravity/campaign GNSS stations. While gravity stations at Port Aransas and

Rockport had permanent GNSS stations located relatively nearby (0.2-4 km, respectively), the permanent GNSS stations nearest to Nueces and Lexington were 10-12 km away, and over 25 km from Packery and Bob Hall. Considering the stations all experienced spatial variability in subsidence rates from one another, it was decided that permanent GNSS stations should not be correlated with the gravity- and campaign GNSS-derived results.

5.2 Conclusion

Land subsidence is a well-known, ongoing problem that negatively impacts the Coastal Bend of Texas. Land subsidence makes coastal communities vulnerable to the effects of global warming, such as sea level rise, which increases the severity and frequency of flooding events. Coastal flooding is associated with coastal erosion, inundation of deltas and emergent land, the inland migration of barrier islands, loss of wetland habitat, and saltwater intrusion in aquifers. Additionally, land subsidence is damaging to urban frameworks such as roads, buildings, sewage systems, and other vital infrastructure. In the Coastal Bend of Texas, land deformation varies across the study area, and it is attributed to sediment compaction, growth faulting, and increased rates of groundwater extraction.

In this study, four different approaches were used for quantifying land subsidence rates over the Coastal Bend of Texas on both local and regional scales. These approaches were integrated in order to create, compare, and validate each dataset. The first approach was a gravity survey, which used a relative gravimeter to measure temporal gravity changes every two weeks for a period of two years (Oct. 2020 – Sept. 2022) on a local scale over six different areas around Corpus Christi, North Padre Island, Mustang Island, and Rockport. The second approach was a campaign GNSS survey carried out alongside the gravity survey, in which coordinates, elevation, and time was recorded. The third approach used InSAR to generate land deformation velocities over the central Coastal Bend area on a regional scale from January 2017 to November 2021. These rates were then mapped in a GIS environment in order to visualize rates and location of deformation. The fourth approach used fifteen permanent GNSS stations to quantify land subsidence rates on a regional scale over a time period similar to that of the InSAR. The gravity and campaign GNSS methods were compared with each other, while the InSAR and permanent GNSS datasets were compared. Integrating these methods allowed for crustal deformation to be quantified around the coastal bend. Factors driving InSAR-derived subsidence rates were also investigated.

Results of this study showed that land subsidence rates exhibited spatial and temporal variations across the Coastal Bend of Texas. Four regions were identified to experience significant InSAR-derived land subsidence rates: coastal towns (6 in total); inland towns (17 in total); cities (6 in total); industrial plants (8 in total). Four coastal towns subsided at an average rate of -2 ± 3 mm/yr, likely driven by sediment compaction and growth faulting. Three inland towns experienced average subsidence rates of -4 ± 4 mm/yr; two inland towns close in proximity to the coastline experienced subsidence that is likely attributed to a high density of growth faults, while the town located further inland could have experienced subsidence due to enhanced groundwater extraction activities. Three areas classified as city around Corpus Christi Proper experienced an average subsidence rate of -1 ± 2 mm/yr, with subsidence being attributed to increased groundwater extraction rates, sediment compaction, and growth faulting. Seven of the industrial plants experienced subsidence at an average rate of -4 ± 6 mm/yr. The localized subsidence observed within these areas is thought to be driven by sediment compaction by overburden from storage tanks.

Quantifying land subsidence is important in estimating climate-related changes in sea-level, determining the local geoid, and supporting coastal communities in mitigating the effects of natural interventions and improving their resilience against these forces. The method and integration technique in this study could be used to aid coastal communities and their policymakers in determining the rates and locations of subsidence and other deformation in order to mitigate the inevitable effects of global warming and coastal flooding.

REFERENCES

Al Mukaimi ME, Dellapenna TM, Williams JR (2018) Enhanced land subsidence in Galveston Bay, Texas: Interaction between sediment accumulation rates and relative sea level rise. Estuar Coast Shelf Sci 207:183–193. https://doi.org/10.1016/J.ECSS.2018.03.023

Aly MH, Zebker HA, Giardino JR, Klein AG (2009) Permanent Scatterer investigation of land subsidence in Greater Cairo, Egypt. Geophys J Int 178:1238–1245. https://doi.org/10.1111/J.1365-246X.2009.04250.X/2/178-3-1238-FIG005.JPEG

Bawden GW, Johnson MR, Kasmarek MC, et al (2012) Investigation of land subsidence in the Houston-Galveston region of Texas by using the Global Positioning System and interferometric synthetic aperture radar, 1993-2000. Sci Investig Rep. https://doi.org/10.3133/SIR20125211

Berardino P, Fornaro G, Lanari R, Sansosti E (2002) A new algorithm for surface deformation monitoring based on small baseline differential SAR interferograms. IEEE Trans Geosci Remote Sens 40:2375–2383. https://doi.org/10.1109/TGRS.2002.803792

Blewitt G, Hammond W, Kreemer C (2018) Harnessing the GPS Data Explosion for Interdisciplinary Science. Eos (Washington DC) 99:. https://doi.org/10.1029/2018EO104623

Casarez IR (2020) Aquifer extents in the coastal lowlands aquifer system regional groundwater availability study area in Texas, Louisiana, Mississippi, Alabama, and Florida, 2020. In: U.S. Geol. Surv. https://www.sciencebase.gov/catalog/item/5dc1bb6be4b069579750e2a4. Accessed 5 Sep 2022

Chowdhury AH, Mace RE (2001) Groundwater Models of the Gulf Coast Aquifer of Texas

Cigna F, Tapete D (2021) Sentinel-1 Big Data Processing with P-SBAS InSAR in the

Geohazards Exploitation Platform: An Experiment on Coastal Land Subsidence and Landslides in Italy. Remote Sens 2021, Vol 13, Page 885 13:885. https://doi.org/10.3390/RS13050885

Crosetto M, Monserrat O, Cuevas-González M, et al (2016) Persistent Scatterer Interferometry: A review. ISPRS J Photogramm Remote Sens 115:78–89. https://doi.org/10.1016/J.ISPRSJPRS.2015.10.011

Dewitz J (2021) National Land Cover Database (NLCD) 2019 Products (ver. 2.0, June 2021). In: U.S. Geol. Surv. https://www.usgs.gov/data/national-land-cover-database-nlcd-2019-products

Dolan AH, Walker IJ (2006) Understanding Vulnerability of Coastal Communities to Climate Change Related Risks. Source J Coast Res III:1316–1323

Don NC, Hang NTM, Araki H, et al (2006) Salinization processes in an alluvial coastal lowland plain and effect of sea water level rise. Environ Geol 49:743–751. https://doi.org/10.1007/S00254-005-0119-7/FIGURES/9

Donaldson EC, Yen TF, Chilingarian GV (1995) Subsidence Due to Fluid Withdrawal: Developments in Petroleum Science. Elsevier Science, Amsterdam

Emanuel K (2005) Increasing destructiveness of tropical cyclones over the past 30 years. Nat 2005 4367051 436:686–688. https://doi.org/10.1038/nature03906

Ewing TE, Anderson RG, Babalola O, et al (1986) Structural Styles of the Wilcox and Frio Growth-Fault Trends in Texas: Cpnstraints on Geopressured Reservoirs. Austin

Farolfi G, Del Soldato M, Bianchini S, Casagli N (2019) A procedure to use GNSS data to calibrate satellite PSI data for the study of subsidence:an example from the north-western Adriatic coast (Italy). https://doi.org/101080/2279725420191663710 52:54–63.

https://doi.org/10.1080/22797254.2019.1663710

Felsenstein D, Lichter M (2014) Social and economic vulnerability of coastal communities to sea-level rise and extreme flooding. Nat Hazards 71:463–491. https://doi.org/10.1007/S11069-013-0929-Y/TABLES/8

Fernández-Martínez M, Vicca S, Janssens IA, et al (2018) The consecutive disparity index, D: a measure of temporal variability in ecological studies. Ecosphere 9:e02527. https://doi.org/10.1002/ECS2.2527

Fitzgerald DM, Fenster MS, Argow BA, Buynevich I V (2008) Coastal Impacts Due to Sea-Level Rise. https://doi.org/10.1146/annurev.earth.35.031306.140139

Galloway DL, Burbey TJ (2011) Review: Regional land subsidence accompanying groundwater extraction. Hydrogeol J 19:1459–1486. https://doi.org/10.1007/S10040-011-0775-5/FIGURES/8

Galloway WE (1986) Growth Faults and Fault-Related Structures of Prograding Terrigenous Clastic Continental Margins. 36:

Guarnieri AM, Guccione P, Pasquali P, Desnos YL (2003) Multi-mode ENVISAT ASAR interferometry: Techniques and preliminary results. IEE Proc Radar, Sonar Navig 150:193–200. https://doi.org/10.1049/IP-RSN:20030516

Haley M, Ahmed M, Gebremichael E, et al (2022) Land Subsidence in the Texas Coastal Bend: Locations, Rates, Triggers, and Consequences. Remote Sens 2022, Vol 14, Page 192 14:192. https://doi.org/10.3390/RS14010192

Hammes U, Loucks RG, Brown LF, et al (2004) Structural Setting and Sequence Architecture of a Growth-Faulted Lowstand Subbasin, Frio Formation, South Texas. Gulf Coast Assoc Geol Soc Trans 54:237–246

Heath JP (2006) Quantifying temporal variability in population abundances. Oikos 115:573. https://doi.org/10.1111/j.2006.0030-1299.15067.x

Hwang C, Cheng TC, Cheng CC, Hung WC (2010) Land subsidence using absolute and relative gravimetry: A case study in central Taiwan. Surv Rev 42:27–39. https://doi.org/10.1179/003962609X451672

Hwang C, Wang CG, Lee LH (2002) Adjustment of relative gravity measurements using weighted and datum-free constraints. Comput Geosci 28:1005–1015. https://doi.org/10.1016/S0098-3004(02)00005-5

Issawy E, Radwan A, DAHY SA, RAYAN A (2010) Monitoring of recent crustal movements around Cairo by repeated gravity and geodetic observations. Contrib to Geophys Geod 173–184

Jackson MPA (1995) Retrospective Salt Tectonics. 1–28

Lanari R, Casu F, Manzo M, et al (2007) An Overview of the Small BAseline Subset Algorithm: A DInSAR Technique for Surface Deformation Analysis. Deform Gravity Chang Indic Isostasy, Tectonics, Volcanism, Clim Chang 637–661. https://doi.org/10.1007/978-3-7643-8417-3_2

Landau H, Vollath U, Chen X (2002) Virtual Reference Station Systems. J Glob Position Syst 1:137–143

Letetrel C, Karpytchev M, Bouin MN, et al (2015) Estimation of vertical land movement rates along the coasts of the Gulf of Mexico over the past decades. Cont Shelf Res 111:42–51. https://doi.org/10.1016/J.CSR.2015.10.018

Liu Y, Li J, Fasullo J, Galloway DL (2020) Land subsidence contributions to relative sea level rise at tide gauge Galveston Pier 21, Texas. Sci Reports 2020 101 10:1–11.

https://doi.org/10.1038/s41598-020-74696-4

Longman IM (1959) Formulas for Computing the Tidal Accelerations Due to the Moon and the Sun. J Geophys Res 64:

Loucks RG (1978) Geothermal resources, Vicksburg Formation, Texas Gulf Coast. https://doi.org/10.2172/6599425

Lu Z, Kwoun O, Rykhus R (2007) Interferometric Synthetic Aperture Radar (InSAR): Its Past, Present and Future Permafrost deformation monitoring and modeling using interferometric synthetic aperture radar (InSAR) in Alaska. View project National Reasearch View project. Photogramm Eng Remote Sensing

Mario Costantini T (1998) A novel phase unwrapping method based on network programming. IEEE Trans Geosci Remote Sens 36:813–821. https://doi.org/10.1109/36.673674

Mcgranahan G, Balk D, Anderson B (2007) The rising tide: assessing the risks of climate change and human settlements in low elevation coastal zones. IIED) 19:17–37. https://doi.org/10.1177/0956247807076960

Moreira A, Prats-Iraola P, Younis M, et al (2013) A tutorial on synthetic aperture radar. IEEE Geosci Remote Sens Mag 1:6–43. https://doi.org/10.1109/MGRS.2013.2248301

Nakagawa I, Satomura M, Seto T, et al (1973) LaCoste&Romberg重力計(G型)の特性について(第1報). 測地学会誌 19:100–112. https://doi.org/10.11366/SOKUCHI1954.19.100

NOAA (2013) National Coastal Population Report

Okeke I, Nguyen Ba D (2006) InSAR Operational and Processing Steps for DEM Generation

Pacheco-Martínez J, Cabral-Cano E, Wdowinski S, et al (2015) Application of InSAR and Gravimetry for Land Subsidence Hazard Zoning in Aguascalientes, Mexico. https://doi.org/10.3390/rs71215868

Paine JG (1993) Subsidence of the Texas coast: inferences from historical and late Pleistocene sea levels. Tectonophysics 222:445–458. https://doi.org/10.1016/0040-1951(93)90363-O

Prati C, Ferretti A, Perissin D (2010) Recent advances on surface ground deformation measurement by means of repeated space-borne SAR observations. J Geodyn 49:161–170. https://doi.org/10.1016/J.JOG.2009.10.011

Psimoulis P, Ghilardi M, Fouache E, Stiros S (2007) Subsidence and evolution of the Thessaloniki plain, Greece, based on historical leveling and GPS data. Eng Geol 90:55–70. https://doi.org/10.1016/J.ENGGEO.2006.12.001

Qu F, Lu Z, Zhang Q, et al (2015) Mapping ground deformation over Houston–Galveston, Texas using multi-temporal InSAR. Remote Sens Environ 169:290–306. https://doi.org/10.1016/J.RSE.2015.08.027

Romberg L& (2004) Instruction Manual Model G&D Gravity Meters

Ross SM (2010) Using Statistics to Summarize Data Sets. Introd Stat 71–143. https://doi.org/10.1016/B978-0-12-374388-6.00003-X

Simms AR, Anderson JB, DeWitt R, et al (2013) Quantifying rates of coastal subsidence since the last interglacial and the role of sediment loading. Glob Planet Change 111:296–308. https://doi.org/10.1016/J.GLOPLACHA.2013.10.002

Space Agency E (2012) → Sentinel-1 eSA’s Radar Observatory Mission for GMeS Operational Services

Stoeser DB, Shock N, Green GN, et al (2005) Geologic Map Database of Texas

Stukey J, Narasimhan B, Srinivasan R Corpus Christi Bay, Galveston Bay, Mission-Aransas Bay, San Antonio Bay, and Sabine Lake Lower-Watershed Multi-year Land-Use and Land Cover Classifications and Curve Numbers TWDB Contract #0804830788

Swanson RL, Thurlow CI (1973) Recent subsidence rates along the Texas and Louisiana coasts as determined from tide measurements. J Geophys Res 78:2665–2671. https://doi.org/10.1029/JC078I015P02665

Texas Water Science Center (USGS TWSC) (2014) Geologic Database of Texas

Timmen L (2010) Absolute and relative gravimetry. Sci Geod - I Adv Futur Dir 1–48. https://doi.org/10.1007/978-3-642-11741-1_1/FIGURES/21

Torge W (1986) Gravimetry for monitoring vertical crustal movements: Potential and problems. Tectonophysics 130:. https://doi.org/10.1016/0040-1951(86)90127-7

van Asselen S, Stouthamer E, van Asch TWJ (2009) Effects of peat compaction on delta evolution: A review on processes, responses, measuring and modeling. Earth-Science Rev 92:35–51. https://doi.org/10.1016/J.EARSCIREV.2008.11.001

Venkataramanan V, Packman AI, Peters DR, et al (2019) A systematic review of the human health and social well-being outcomes of green infrastructure for stormwater and flood management. J Environ Manage 246:868–880. https://doi.org/10.1016/J.JENVMAN.2019.05.028

Wahr J (1995) Earth Tides. In: Ahrens TJ (ed) Global Earth Physics: A Handbook of Physical Constraints. American Geophysical Union (AGU), pp 40–46

Walker JP, Houser PR, Willgoose GR (2004) Active microwave remote sensing for soil moisture measurement: a field evaluation using ERS-2. Hydrol Process 18:1975–1997. https://doi.org/10.1002/HYP.1343

Wang G, Asce M (2021) The 95% Confidence Interval for GNSS-Derived Site Velocities. J Surv Eng 148:04021030. https://doi.org/10.1061/(ASCE)SU.1943-5428.0000390

Warrick RA, Oerlemans J (1990) Sea level rise. Clim Chang IPCC Sci Assess 263–264

Wegmüller U, Werner CL, Strozzi T, Wiesmann A Phase Unwrapping with GAMMA ISP Phase Unwrapping with GAMMA ISP Technical Report, 13-May-2002

Wu SY, Yarnal B, Fisher A (2002) Vulnerability of coastal communities to sea-level rise: a case study of Cape May County, New Jersey, USA. Clim Res 22:255–270. https://doi.org/10.3354/CR022255

Young SC, Ewing PGT, Hamlin S, et al (2012) Final Report Updating the Hydrogeologic Framework for the Northern Portion of the Gulf Coast Aquifer Texas Water Development Board

Yu J, Wang G (2016) Introduction to the GNSS geodetic infrastructure in the Gulf of Mexico Region. http://dx.doi.org/101080/0039626520151108069 49:51–65. https://doi.org/10.1080/00396265.2015.1108069

Yuill B, Lavoie D, Reed DJ (2009) Understanding Subsidence Processes in Coastal Louisiana. J Coast Res 10054:23–36. https://doi.org/10.2112/SI54-012.1

Zebker HA, Villasenor J (1992) Decorrelation in Interferometric Radar Echoes

Zhou X, Wang G, Wang K, et al (2021) Rates of Natural Subsidence along the Texas Coast Derived from GPS and Tide Gauge Measurements (1904–2020). J Surv Eng 147:04021020. https://doi.org/10.1061/(asce)su.1943-5428.0000371

(2021) SBAS Tutorial